




## Article

# Computational Modeling of Latent Heat Thermal Energy Storage in a Shell-Tube Unit: Using Neural Networks and Anisotropic Metal Foam

Jana Shafi <sup>1,\*</sup> , Mehdi Ghalambaz <sup>2</sup> , Mehdi Fteiti <sup>3</sup>, Muneer Ismael <sup>4</sup> and Mohammad Ghalambaz <sup>5</sup> 

- <sup>1</sup> Department of Computer Science, College of Arts and Science, Prince Sattam Bin Abdul Aziz University, Wadi Ad-Dawasir 11991, Saudi Arabia
- <sup>2</sup> Institute of Research and Development, Duy Tan University, Da Nang 550000, Vietnam
- <sup>3</sup> Physics Department, Faculty of Applied Sciences, Umm Al-Qura University, Makkah 24381, Saudi Arabia
- <sup>4</sup> Mechanical Engineering Department, Engineering College, University of Basrah, Basrah 61004, Iraq
- <sup>5</sup> Laboratory on Convective Heat and Mass Transfer, Tomsk State University, 634045 Tomsk, Russia
- \* Correspondence: j.jana@psau.edu.sa

**Abstract:** Latent heat storage in a shell-tube is a promising method to store excessive solar heat for later use. The shell-tube unit is filled with a phase change material PCM combined with a high porosity anisotropic copper metal foam (FM) of high thermal conductivity. The PCM-MF composite was modeled as an anisotropic porous medium. Then, a two-heat equation mathematical model, a local thermal non-equilibrium approach LTNE, was adopted to consider the effects of the difference between the thermal conductivities of the PCM and the copper foam. The Darcy–Brinkman–Forchheimer formulation was employed to model the natural convection circulations in the molten PCM region. The thermal conductivity and the permeability of the porous medium were a function of an anisotropic angle. The finite element method was employed to integrate the governing equations. A neural network model was successfully applied to learn the transient physical behavior of the storage unit. The neural network was trained using 4998 sample data. Then, the trained neural network was utilized to map the relationship between control parameters and melting behavior to optimize the storage design. The impact of the anisotropic angle and the inlet pressure of heat transfer fluid (HTF) was addressed on the thermal energy storage of the storage unit. Moreover, an artificial neural network was successfully utilized to learn the transient behavior of the thermal storage unit for various combinations of control parameters and map the storage behavior. The results showed that the anisotropy angle significantly affects the energy storage time. The melting volume fraction MVF was maximum for a zero anisotropic angle where the local thermal conductivity was maximum perpendicular to the heated tube. An optimum storage rate could be obtained for an anisotropic angle smaller than 45°. Compared to a uniform MF, utilizing an optimum anisotropic angle could reduce the melting time by about 7% without impacting the unit's thermal energy storage capacity or adding weight.



**Citation:** Shafi, J.; Ghalambaz, M.; Fteiti, M.; Ismael, M.; Ghalambaz, M. Computational Modeling of Latent Heat Thermal Energy Storage in a Shell-Tube Unit: Using Neural Networks and Anisotropic Metal Foam. *Mathematics* **2022**, *10*, 4774. <https://doi.org/10.3390/math10244774>

Academic Editors: Yuan Dong and Yuchao Hua

Received: 5 December 2022

Accepted: 13 December 2022

Published: 15 December 2022

**Publisher's Note:** MDPI stays neutral with regard to jurisdictional claims in published maps and institutional affiliations.

**Keywords:** computational modeling; finite element method; neural networks; anisotropic metal foam; thermal energy storage

**MSC:** 76R10; 80A22; 80M10



**Copyright:** © 2022 by the authors. Licensee MDPI, Basel, Switzerland. This article is an open access article distributed under the terms and conditions of the Creative Commons Attribution (CC BY) license (<https://creativecommons.org/licenses/by/4.0/>).

## 1. Introduction

Thermal energy storage (TES) has found essential applications in the automotive, power generation, buildings, and food industries [1]. TES technology has shown great potential to regulate the difference between the supply and demand chain. TES technology promotes the flexibility, efficiency, and reliability of thermal energy systems by regulating real-world heat sources' fluctuation and intermittency nature [2]. Latent thermal energy storage (LHTES) utilizes the latent heat of fusion and store/release thermal energy at a

constant temperature in a compact space. Thus, LHTES systems are promising for large- and small-scale applications. LHTES units have been utilized in buildings [3,4], solar systems [5], solar air heating [6], solar dryers [7], and waste heat recovery [8].

Although LHTES systems can store/release a considerable amount of latent heat at a constant fusion temperature, they suffer from poor thermal conductivity of conventional phase change material (PCM) [5,9]. Thus various methods, such as using fins [10–12], nanoparticles [13,14], metal foams [15,16], or a combination of these methods [17]. Embedding PCMs in open-cell metal foams is an excellent approach for improving the heat transfer performance of LHTES systems, which has attracted the attention of recent researchers [18]. However, metal foams do not undergo a phase change and cannot contribute to latent heat TES. Moreover, metal foams are made of thermally conductive metals such as copper, aluminum, and nickel, which increase the cost and weight of the LHTES unit. Thus, some researchers tried to utilize layers of metal foam to improve the system's thermal performance by using a minimum amount of metal foam.

For example, Zhang et al. [19] experimentally investigated the influence of using layers of metal foams in an enclosure. They also investigated the impact of utilizing different layers of metal foam on the heat transfer behavior of an LHTES unit. The results showed that filling the enclosure with metal foam up to 5/6 of its capacity improves heat transfer. Using different types of foam layers could also improve heat transfer. A metal foam layer with a high porosity should be placed next to the heated wall or at the top regions of the enclosure unit. Buonomo et al. [20] studied the effect of a metal foam layer on the thermal performance of a shell-tube shape LHTES unit where the foam layer was placed on the tube. The authors examined the effect of various porosities in the range of 0.9–0.97 and various foam thicknesses on the melting time. An increase in the thickness of the foam layer could change the heat transfer regimes and reduce the melting time. Ge et al. [21] utilized several optimized shapes of fins in a horizontal shell-tube shape thermal energy storage. They compared the advantage of fins with metal foams. They reported that using fins or metal foams (fully or half-filled enclosures) could improve the heat transfer rate by 3.3–5.8 times. They demonstrated that the topology-optimized fins could provide better thermal enhancement compared to metal foams. However, the production cost of optimized fins was higher. Hashem Zadeh et al. [22] utilized different configurations of fin shape layers of metal foams to improve heat transfer in a horizontal shell-tube shape LHTES unit. A Y shape design could produce the best charging performance.

Some researchers tried to change the structure of metal foams and produce anisotropic metal foams with improved thermal conductivity in a direction. In this approach, the amount of metal foam is fixed, and the changes are applied to the internal structure of the foam. Bamdezh et al. [23] examined the metal foam anisotropy on the thermal behavior of a thermal management system. The authors reported that an increase in the tangential conductance raises the phase change rate. Moreover, promoting axial thermal conductivity enhances heat transfer. Yu et al. [24] explored the anisotropic properties of porous media with two different pore structures and found anisotropic characteristics important. Ren et al. [25] reported the anisotropic thermal conductivity effects in a woven metal foam PCM composite. They reported a better thermal performance for an anisotropic than an isotropic for thermal energy storage applications. They found that a metal foam with engineered anisotropic properties could notably promote heat transfer performance and required material.

The few available literature works on anisotropic metal foams reveal the potential advantage of these materials for LHTES. However, there are only a few experimental or numerical investigations on the engineering design of LHTES units with anisotropic metal foams. The literature review showed that shell-tube type LHTES has many applications in solar energy storage systems. Thus, the present study aims to address the impact of foam anisotropic characteristics on the phase change behavior of shell-tube LHTES units for the first time.

## 2. Mathematical Model

A shell-tube type latent heat thermal energy storage stores/releases thermal energy in thermodynamic cycles. For example, Figure 1 illustrates a view of a solar water heating system. In this system, a cold-water source supplies the building's water demand. The cold water enters a hot water storage tank, providing hot water to the house. The water in the tank circulates in a cycle and goes through solar collectors in a solar heating cycle as water absorbs solar heat and its temperature rises. The excess solar energy can be stored in a compact space, an LHTES unit, in the form of sensible and latent heat. Thus, an LHTES cycle circulates the tanks' hot water in the LHTES units and charges the PCMs inside the unit. Later, at any point, some of the tank's water can be consumed by the building, and cold fresh water will enter the tank, causing a significant temperature drop in the hot water tank. In this case, the LHTES cycle circulates the middle-temperature water of the tank in the LHTES unit. Thus, the PCM in the unit releases its energy to the water and undergoes a solidification process.

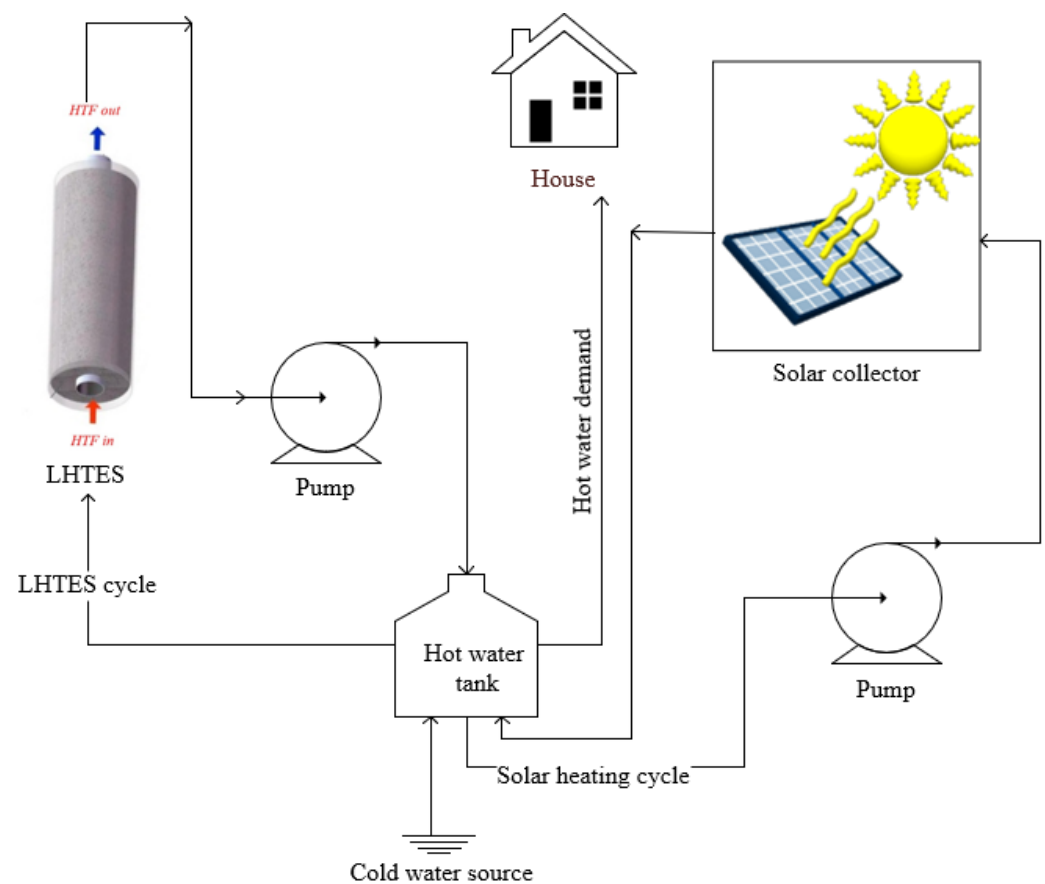


**Figure 1.** A solar water heating cycle for domestic use.

The heat transfer capabilities of the LHTES unit is an important factor in thermodynamic cycles since it dictates the required time to regulate the tank's temperature. Here, it assumed that the thermal charging of LHTES is set at 70 °C, and the LHTES loops activate at this temperature. Thus, by neglecting the line energy losses, the inlet temperature to LHTES can be considered 70 °C.

The storage capacity of the cycle can be adjusted by using several parallel LHTES units. Since the units can be mounted in parallel, their thermal behavior can be similar, and thus, the present study focuses on the modeling and analysis of just one LHTES unit. A schematic view of the LHTES unit is depicted in Figure 2. A shell-tube storage unit is filled by the anisotropic copper foam of porosity  $\varepsilon$ . The thermal conductivity ( $k$ ) and permeability ( $\kappa$ ) of metal foam (MF) can be changed in perpendicular directions. The MF is filled by paraffin with a melting temperature of  $T_f$ . The tube is made of copper with a nominal diameter of  $D = (\frac{1}{2})''$

or  $D = (2.54/2)$  cm [26]. A relative pressure  $P_{in}$  drives the HTF water into the HTF tube at an entrance temperature of  $T_h$ . The LHTES unit is initially at a supper cold temperature  $T_c$ . The tube’s outside diameter, inside diameter, and wall thickness are 1.59 cm, 1.34 cm, and 0.13 cm, respectively. The geometrical details of the shell are reported in Figure 1 as a function of tube nominal radius ( $R = D/2$ ).

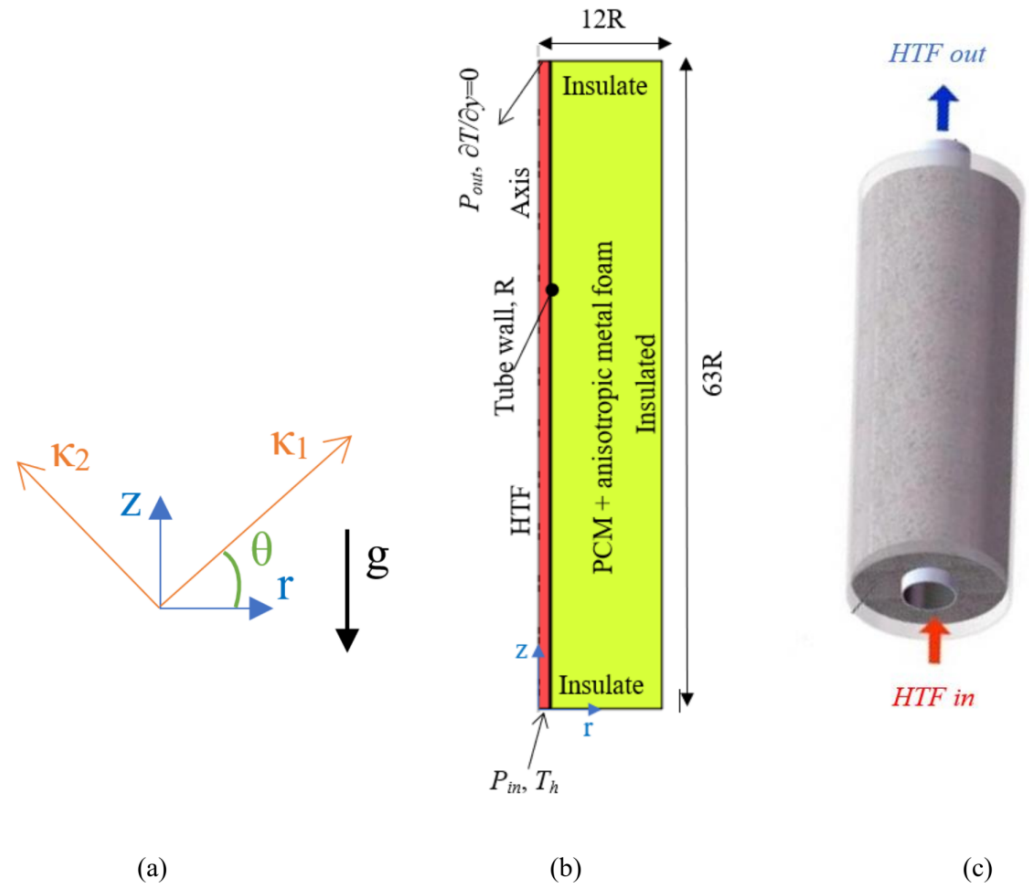


**Figure 2.** A schematic view of the LHTES model with anisotropic MF; (a) the anisotropic alignment; (b) a 2D axis-symmetric view of the shell-tube of the physical model; (c) a 3D view of the model.

2.1. Governing Equations

There are three regions of HTF, copper tube wall, and composite MF-PCM, which are physically coupled. The governing equation for the copper wall is the conduction heat transfer which can be written as in a cylindrical coordinate system:

$$(\rho C_p)_{Wall} \frac{\partial T}{\partial t} = k_{Wall} \frac{\partial^2 T}{\partial z^2} + \frac{k_{Wall}}{r} \frac{\partial}{\partial r} \left( r \frac{\partial T}{\partial r} \right) \tag{1}$$

where  $\rho$ ,  $C_p$ , and  $k$  are the tube wall’s density, specific heat capacity, and thermal conductivity, respectively. Moreover,  $T$  and  $t$  are the temperature field and time, respectively. The cylindrical coordinate system is introduced by the  $r$ - and  $z$ -axis, as indicated in Figure 1. The subscript wall indicates the copper wall.

The governing equations for the HTF region are the continuity, momentum, and convection heat transfer as follows:

$$\frac{\partial u_z}{\partial z} + \frac{1}{r} \frac{\partial (ru_r)}{\partial r} = 0 \tag{2}$$



$$\begin{aligned} \rho_{HTF} \left( \frac{\partial u_r}{\partial t} + u_z \frac{\partial u_r}{\partial z} + u_r \frac{\partial u_r}{\partial r} \right) &= - \left( \frac{\partial p}{\partial r} \right) + \mu_{HTF} \frac{\partial^2 u_r}{\partial z^2} + \frac{\mu_{HTF}}{r} \frac{\partial}{\partial r} \left( r \frac{\partial u_r}{\partial r} \right) - \frac{\mu_{HTF} u_r}{r^2} \\ \rho_{HTF} \left( \frac{\partial u_z}{\partial t} + u_z \frac{\partial u_z}{\partial z} + u_r \frac{\partial u_z}{\partial r} \right) &= - \left( \frac{\partial p}{\partial z} \right) + \mu_{HTF} \frac{\partial^2 u_z}{\partial z^2} + \frac{\mu_{HTF}}{r} \frac{\partial}{\partial r} \left( r \frac{\partial u_z}{\partial r} \right) \end{aligned} \tag{3}$$

$$(\rho C_p)_{HTF} \left( \frac{\partial T}{\partial t} + u_z \frac{\partial T}{\partial z} + u_r \frac{\partial T}{\partial r} \right) = k_{HTF} \frac{\partial^2 T}{\partial z^2} + \frac{k_{HTF}}{r} \frac{\partial}{\partial r} \left( r \frac{\partial T}{\partial r} \right) \tag{4}$$

where the velocity components in the  $r$  and  $z$  directions are denoted by  $u_r$  and  $u_z$ , respectively. The fluid’s dynamic viscosity is  $\mu$ , and the subscript HTF represents the heat transfer liquid. Here, it was assumed that the thermophysical properties are constant. Moreover, the fluid flow is laminar ( $Re_{HTF} < 2000$ ) where  $Re_{HTF} = \rho_{HTF} \times u \times D / \mu_{HTF}$ , and  $u = \sqrt{u_r^2 + u_z^2}$ . It should be noted that there is no gravity effect in the HTF governing equations since it was assumed that the HTF works in a closed loop, and the static pressure does not contribute to the fluid movement.

Regarding the composite MF-PCM, the metal foam is made of open cells, and thus the liquid PCM can move inside the pores. In the molten PCM, there are temperature gradients; hence, the buoyancy forces can induce natural convection flow circulation. Thus, the continuity and momentum equations should be solved along with the phase change heat equation to simulate the natural convection heat transfer with phase change. Here, the enthalpy porosity formulation is used to simulate phase change. Source terms as a function of melt volume fraction ( $\varphi$ ) are added to the momentum equation to force velocities to zero in solid regions. Here, a difference between the temperature of MF porous matrix ( $T_{MF}$ ) and the temperature of the PCM ( $T_{PCM}$ ) inside the pores was considered. Thus, a local-thermal non-equilibrium (LTNE) model was used to explain the temperature differences. Considering the non-Darcy effects and controlling source terms, the governing equations for continuity, momentum, and phase change heat transfer can be expressed as follows [27–29]:

$$\frac{\partial u_z}{\partial z} + \frac{1}{r} \frac{\partial (r u_r)}{\partial r} = 0 \tag{5}$$

$$\begin{aligned} \frac{\rho_{PCM}}{\varepsilon} \frac{\partial u_r}{\partial t} + \frac{\rho_{PCM}}{\varepsilon^2} \left( u_z \frac{\partial u_r}{\partial z} + u_r \frac{\partial u_r}{\partial r} \right) &= - \left( \frac{\partial p}{\partial r} \right) + \frac{\mu_{PCM}}{\varepsilon} \left[ \frac{\partial^2 u_r}{\partial z^2} + \frac{1}{r} \frac{\partial}{\partial r} \left( r \frac{\partial u_r}{\partial r} \right) - \frac{u_r}{r^2} \right] \\ &\quad - \frac{\mu_{PCM}}{\kappa} u_r - \rho_{PCM} \frac{C_F}{\sqrt{\kappa}} |u| u_r + A_{mush} \frac{(1-\varphi(T))^2}{\lambda_{mush} + \varphi^3(T)} u_r \end{aligned} \tag{6a}$$

$$\begin{aligned} \frac{\rho_{PCM}}{\varepsilon} \frac{\partial u_z}{\partial t} + \frac{\rho_{PCM}}{\varepsilon^2} \left( u_z \frac{\partial u_z}{\partial z} + u_r \frac{\partial u_z}{\partial r} \right) &= - \left( \frac{\partial p}{\partial z} \right) + \frac{\mu_{PCM}}{\varepsilon} \left[ \frac{\partial^2 u_z}{\partial z^2} + \frac{1}{r} \frac{\partial}{\partial r} \left( r \frac{\partial u_z}{\partial r} \right) \right] \\ &\quad + g \rho_{PCM} \beta_{PCM} (T - T_0) - \frac{\mu_{PCM}}{\kappa} u_z - \rho_{PCM} \frac{C_F}{\sqrt{\kappa}} |u| u_z + A_{mush} \frac{(1-\varphi(T))^2}{\lambda_{mush} + \varphi^3(T)} u_z \end{aligned} \tag{6b}$$

$$\begin{aligned} \varepsilon (\rho C_p)_{PCM} \frac{\partial T_{PCM}}{\partial t} + (\rho C_p)_{PCM} \left( u_z \frac{\partial T_{PCM}}{\partial z} + u_r \frac{\partial T_{PCM}}{\partial r} \right) &= \\ \frac{\partial}{\partial z} \left( k_{eff, PCM} \frac{\partial T_{PCM}}{\partial z} \right) + \frac{1}{r} \frac{\partial}{\partial r} \left( k_{eff, PCM} r \frac{\partial T_{PCM}}{\partial r} \right) &+ h_v (T_{MF} - T_{PCM}) - \varepsilon \rho_{PCM} L_{PCM} \frac{\partial \varphi(T)}{\partial t} \end{aligned} \tag{7a}$$

$$(1 - \varepsilon) (\rho C_p)_{MF} \frac{\partial T_{MF}}{\partial t} = \frac{\partial}{\partial z} \left( k_{eff, MF} \frac{\partial T_{MF}}{\partial z} \right) + \frac{1}{r} \frac{\partial}{\partial r} \left( k_{eff, MF} r \frac{\partial T_{MF}}{\partial r} \right) - h_v (T_{MF} - T_{PCM}) \tag{7b}$$

where  $\kappa$  and  $C_F$  are the porous permeability and Frochheimer parameter, respectively. The volumetric interstitial heat transfer coefficient ( $h_v$ ) is introduced later using the pore scale Nusselt number. The subscripts MF and eff denoted the metal foam and effective properties, respectively. The symbols  $\beta$ ,  $g$ , and  $L$  denote the thermal volume expansion coefficient, gravity acceleration, and latent heat of fusion, respectively. The source terms containing  $A_{mush}$  and  $\lambda_{mush}$  force the fluid velocity to zero in the solid regions. Thus, a substantial value of  $A_{mush} = 10^{10}$  Pa.s/m<sup>2</sup> was adopted to adequately force the fluid velocities to zero by dominating the flow solution in solid regions.

Moreover,  $\lambda_{mush} = 0.001$  was used to avoid a zero denominator in the source terms. The dynamic viscosity was considered as a function of melt fraction ( $\varphi$ ) to better control the solver stability and force the velocity to zero in solid regions. Thus, the viscosity was

introduced as  $\mu_{PCM} = \varphi \times \mu_{PCM,l} + (1 - \varphi) \times \mu_a$  where  $\mu_a$  is an artificially large viscosity value. It was adopted as  $10^4$  Pa.s in the current study. Using this formula, the viscosity tends to the typical dynamic viscosity  $\mu_{PCM,l}$  when  $\varphi = 1$  (liquid region), and it artificially increases to a substantial value in a solid region ( $\varphi = 0$ ). Since the aim of source terms is to force the velocities to zero in a solid region, the artificial increase in the dynamic viscosity helps force the velocities to zero in a solid region. Moreover, such a dynamic viscosity formulation helps with the solver stability and facilitates numerical computations without impacting the physical model.

Equation (7a,b) represent heat transfer in the PCM and MF phases. The term  $h_v (T_{MF} - T_{PCM})$  considers the thermal interaction of two phases. The effective thermal conductivities for PCM and MF are used in these equations since the pore structures influence these thermal conductivities [30]. Melting volume fraction,  $\varphi$ , is a function of PCM temperature as [31]:

$$\varphi(T) = \begin{cases} 0 & T < T_f - 0.5\Delta T_f \text{ (Solid phase)} \\ 0.5 + \frac{(T-T_f)}{\Delta T_f} & T_f - 0.5\Delta T_f \leq T \leq T_f + 0.5\Delta T_f \text{ (Mushy region)} \\ 1 & T > T_f + 0.5\Delta T_f \text{ (Liquid phase)} \end{cases} \quad (8)$$

where  $\Delta T_f$  is the phase transition interval around the fusion temperature  $T_f$ . MF's thermal conductivity and permeability are anisotropic, and they can change in perpendicular directions. Supporting the MF ligaments in one direction enhances the thermal conductivity with the cost of reducing MF permeability. Hence, they have been introduced using a second-order tensor follows [32]:

$$\kappa = \begin{bmatrix} \kappa_2(\sin \theta)^2 + \kappa_1(\cos \theta)^2 & (\kappa_1 - \kappa_2)(\cos \theta)(\sin \theta) \\ (\kappa_1 - \kappa_2)(\cos \theta)(\sin \theta) & \kappa_2(\cos \theta)^2 + \kappa_1(\sin \theta)^2 \end{bmatrix} \quad (9a)$$

$$k_{\text{eff,MF}} = \begin{bmatrix} k_2(\sin \theta)^2 + k_1(\cos \theta)^2 & (k_1 - k_2)(\sin \theta)(\cos \theta) \\ (k_1 - k_2)(\sin \theta)(\cos \theta) & k_2(\cos \theta)^2 + k_1(\sin \theta)^2 \end{bmatrix} \quad (9b)$$

where  $\kappa_1 = (1 - \zeta) \times \kappa_a$ ,  $\kappa_2 = (1 + \zeta) \times \kappa_a$ ,  $k_1 = (1 + \zeta) \times k_a$ , and  $k_2 = (1 - \zeta) \times k_a$ . The anisotropic angle,  $\theta$ , is defined in Figure 2b, and it represents the angle of anisotropic MF placement in the enclosure. Here,  $\zeta$  is the anisotropic factor, where  $\zeta = 0$  represents an isotropic MF. The anisotropic factor ( $\zeta$ ) cannot be too high since the MF should stay connected and continuous. Thus, in the present study, the anisotropic factor is adopted as a moderate value of  $\zeta = 0.2$  [32]. The average permeability ( $\kappa_a$ ) [33] and average MF effective thermal conductivity ( $k_a$ ) of the MF are computed using [27,30]:

$$k_a = \frac{1 - \varepsilon}{3} k_{\text{MF}} \quad (10a)$$

$$\kappa_a = \frac{\varepsilon^2 \left( d_{fp} \sqrt{\frac{\kappa_{\text{tor}}}{3\varepsilon}} \right)^2}{36(\kappa_{\text{tor}} - 1)\kappa_{\text{tor}}} \quad (10b)$$

where  $k_{\text{MF}}$  is the bulk thermal conductivity of MF material and  $d_{fp}$  and  $\kappa_{\text{tor}}$  are introduced as [33]:

$$d_{fs} = 1.18 \sqrt{\frac{1 - \varepsilon}{3\pi}} \left\{ \frac{1}{1 - e^{\frac{(\varepsilon-1)}{0.04}}} \right\} d_{fp} \quad (11a)$$

$$\frac{1}{\kappa_{\text{tor}}} = \frac{3}{4\varepsilon} + \frac{\sqrt{9 - 8\varepsilon}}{2\varepsilon} \cos \left\{ \frac{4\pi}{3} + \frac{1}{3} \cos^{-1} \left( \frac{8\varepsilon^2 - 36\varepsilon + 27}{(9 - 8\varepsilon)^{\frac{3}{2}}} \right) \right\} d_{fp} \quad (11b)$$

in which,  $d_{fp}$  is computed using MF pore per inch (PPI) property as [33]:

$$d_{fp} = \frac{0.0254}{PPI} \quad (11c)$$

The Frochheimer parameter is computed using [33]:

$$C_F = 0.00212(1 - \varepsilon)^{-0.132} \left( \frac{d_{fs}}{d_{fp}} \right)^{-1.63} \tag{12}$$

The heat exchange between the PCM and MF was evaluated using the volumetric interstitial heat transfer coefficient as [34]:

$$h_v = Nu_v \frac{k_{PCM}}{d_{fs}^2} \tag{13}$$

where  $Nu_v$  is the interstitial heat transfer Nusselt number introduced in a volumetric form [35]. Then,  $Nu_v$  is computed for low pore scale Reynold numbers as [34]:

$$Nu_v = \begin{cases} 76.99 - 152.01\varepsilon + 75.04\varepsilon^2 & 0 \leq Re \leq 0.1 \\ (1.72 + 1.71\varepsilon - 3.46\varepsilon^2)Re^{0.26}Pr^{0.28} & 0.1 < Re \leq 1 \end{cases} \tag{14}$$

where  $Pr = \rho_{PCM} \times \mu_{PCM} / \alpha_{PCM}$  and  $\alpha_{PCM} = k_{PCM} / (\rho C_p)_{PCM}$ . The pore scale Reynold number ( $Re$ ) was also introduced as  $Re = \rho_{PCM} \times u_{PCM} \times d_{fs} / \mu_{PCM}$ . Many past literature studies used different relations to estimate the Nusselt number. However, most of the available relationships are related to high values of the Reynolds number and typically  $Re > 1$ . However, for the natural convection of PCM in MF, the circulation velocities are small, and  $Re$  is typically smaller than unity. Thus, a relation for the specific range of  $Re < 1$  should be used. Therefore, here, the relation reported by Yao et al. [34] was adopted. This relation was tested against the experimental observations and agreed well with the phase change in PCMs in MF. Equation (16) holds for  $21 < Pr < 41$  and  $0.929 < \varepsilon < 0.974$ . Moreover, it should be noted that the heat transfer exchange ( $Nu_v$ ) is not zero when the velocity is very small or zero since there is still an active thermal diffusion heat transfer which can play a significant role in the thermal exchange between the PCM and MF phases.

Finally, the effective thermal conductivity of PCM was also evaluated [27,30]:

$$k_{eff,PCM} = \frac{2 + \varepsilon}{3} k_{PCM} \tag{15a}$$

A linear weight average was used to compute the thermophysical properties of the PCM in the mushy region:

$$(\rho C_p)_{PCM} = (1 - \varphi)(\rho C_p)_l + \varphi(\rho C_p)_s \tag{15b}$$

$$\rho_{PCM} = (1 - \varphi)\rho_l + \varphi\rho_s \tag{15c}$$

where subscripts l and s indicate the PCM in the liquid and solid phases. Table 1 summarizes the thermophysical properties of the tube, MF, and paraffin.

**Table 1.** Thermophysical properties of PCM, metal foam, and HTF fluid.

Materials	K (W/m.K)	$\rho$ (kg/m <sup>3</sup> )	$c_p$ (J/kg.K)	$T_m$ (°C)	L (kJ/kg)	$\mu_f$ (kg/m.s)	B (1/K)
Paraffin (solid/liquid) [36–38]	0.21/0.12	916/790	2700/2900	49–54	176	0.0036	0.00091
Copper foam [39]	380	8900	386	-	-	-	-
Water [40]	0.613	997.1	4179	-	-	0.000957	0.00021

### 2.2. Initial and Boundary Conditions

The continuity of temperature and heat flux was considered for all coupled interfaces. For the MF region with LTNE conditions, the continuity of temperature was applied. For the continuity of the heat flux ( $q$ ), it was divided into two parts based on the volume fraction of each phase (porosity). Thus, the heat flux continuity at the interface of the tube wall and MF region was introduced as:

$$q_{\text{Wall}} = \varepsilon q_{\text{MF}} + (1 - \varepsilon)q_{\text{PCM}} \tag{16}$$

A uniform inlet temperature of  $T_h$  was applied as  $T = 70$  °C. A constant relative pressure for  $p = P_{in}$  was applied at the HTF inlet boundary. The outflow condition with a relative pressure zero and  $-n \cdot q = 0$  was applied at the outlet where  $n$  is the normal vector to a surface. The shell walls are assumed well insulated with  $-n \cdot q = 0$ . The no-slip and impermeability boundary conditions were employed for all boundary surfaces except the inlet and outlet boundaries which were explained. The entire LHTES unit was assumed at an initial temperature of  $T_c = 14$  °C. A reference pressure point with zero relative pressure was considered at the bottom left corner of the shell space. The thermophysical properties of HTF fluid (water) and copper foam can be varied slightly by temperature variations.

Since the temperature variation is limited in the present study, the thermophysical properties were assumed constant except for the phase change material which undergoes a phase change. Moreover, the impact of the temperature variations on the density change was included in the buoyancy effect using the Boussinesq model in the liquid PCM.

### 2.3. Characteristics Parameters

The melting volume fraction shows the average amount of molten PCM in the enclosure, and it was defined as:

$$MV_F = \frac{\int_V \varepsilon \phi dV}{\int_V \varepsilon dV} \tag{17}$$

where  $dV$  is the volume element of the shell domain. The average outlet temperature difference is introduced as:

$$\Delta T = T_h - \frac{\int_A u_z T dA}{\int_A u_z dA} \tag{18}$$

where  $A$  is the surface area of the outlet. The stored thermal energy was computed as the sum of sensible and latent heat:

$$Q_{\text{sensible}} = \left[ \int_V \left( \int_{T_0}^T \varepsilon (\rho C_P)_{\text{PCM}}(T) dT \right) dV \right] + (T - T_0)(\rho C_P)_{\text{MF}} \int_V (1 - \varepsilon) dV + (T - T_0)(\rho C_P)_{\text{Wall}} V_{\text{Wall}} + (T - T_0)(\rho C_P)_{\text{HTF}} V_{\text{HTF}} \tag{19}$$

$$Q_{\text{latent}} = \varepsilon \int_V \rho_{\text{PCM}} \phi L_{\text{PCM}} dV \tag{20}$$

$$Q_{\text{store}} = Q_{\text{sensible}} + Q_{\text{latent}} \tag{21}$$

The average velocity of HTF ( $u_a$ ) leaving the unit is computed as  $u_a = \int_A u_z dA / \int_A dA$ . It should be noted that the present study is an axis-symmetric model, and the 2D lines are axis-symmetric surfaces, and the 2D surfaces are indeed axis-symmetric volumes. Using the HTF average velocity, the HTF tube Reynolds number ( $Re_{\text{HTF}}$ ) is introduced as  $Re_{\text{HTF}} = \rho_{\text{HTF}} \times u_a(D_{in}) / \mu_{\text{HTF}}$  where  $D_{in}$  is the inside diameter of the HTF tube.

Energy storage power

$$\text{Power} = Q_{\text{store}}/t \tag{22}$$

The energy storage power indicates the average power of thermal energy storage from the initial state (super cold PCM) to any given time during the charging process.

### 3. Solution Method

#### 3.1. Numerical Method

The governing equations in each domain are integrated over a structured mesh using the finite element method [41] in their weak form to obtain a set of residual equations. In the present governing equations, there are strong multi-physics non-linear source/sink terms due to the phase change effects. Thus, a numerical method capable of dealing with such non-linearities should be utilized. Here, the finite element provides a smooth, accurate, and continuous approximate solution over mesh elements, which is suitable for the purpose of the present study.

In the finite element method, the Gauss quadrature integration over the linear shape function discretization was used. The field variables are introduced using shape functions at each time step as:

$$\begin{aligned} u_r &\approx \sum_{i=1}^N u_{r,i} \gamma_i(r, z), u_z \approx \sum_{i=1}^N u_{z,i} \gamma_i(r, z), p \approx \sum_{i=1}^N p_i \gamma_i(r, z), \\ T &\approx \sum_{i=1}^N T_i \gamma_i(r, z), T_{MF} \approx \sum_{i=1}^N T_{MF,i} \gamma_i(r, z), T_{PCM} \approx \sum_{i=1}^N T_{PCM,i} \gamma_i(r, z), \end{aligned} \quad (23)$$

where  $\gamma$  is the shape function and  $N$  is the number of discretized regions. The finite element algebraic equations were computed by inserting the above-filed variables into the weak form of the governing equations. Then, the algebraic equations were solved using the Newton method to find the variable fields.

The PARDISO parallel solver [42,43] was invoked to solve the residual equations over multiple computational cores. A constant Newtonian damping factor of 0.9 and relative error tolerance of  $10^{-4}$  were utilized. The solution time steps and convergence were automatically controlled to regulate solution errors within the predefined error tolerance ( $10^{-4}$ ) by the first-second order backward differential formula (BDF) [44]. The convergence of the numerical method was monitored through the evaluation of the residual equations. The BDF scheme monitors the convergence solution at each time step for a relative error to remain in the specific threshold and also to select the next time step. The computations were commenced by employing the initial conditions and continued with the computation of the model parameters. The continuity, momentum, and phase change heat equations are integrated and solved in a fully coupled method. A stop condition of  $MVF \geq 0.999$  was added to terminate the computations when a completed melting condition reaches.

The solution steps are summarized in a flow chart depicted in Figure 3.

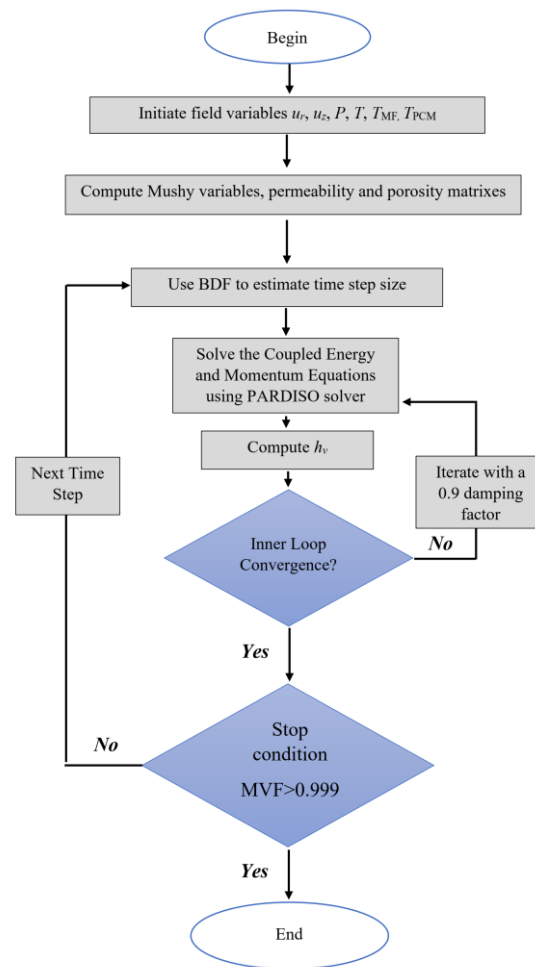


Figure 3. The numerical steps of the unsteady simulations using the finite element method.

Moreover, the momentum equations in the HTF tube were solved as a steady-state step since they are independent of the thermal operating conditions of the LHTES unit. Then, the computed velocities were used in the time-dependent simulations as constant initial values. This step reduces the computational costs without affecting the simulation results.

### 3.2. Mesh Study

A non-uniform unstructured mesh was created in the HTF domain. Moreover, the wall and PCM regions were meshed using a uniform, unstructured mesh. A view of the utilized mesh is displayed in Figure 4.

The number of mesh cells in each domain was  $45N_m \times 5N_m$  (HTF),  $45N_m \times N_m$  (Tube wall), and  $45N_m \times 30N_m$  (PCM). The mesh in the HTF domain was stretched from the tube wall toward the axis with an element ratio of 10. The simulations were repeated for four cases with  $N_m$  equal to 2, 3, 4, and 5 when  $P_{in} = 5 \text{ Pa}$ ,  $\zeta = 0.2$ , and  $\theta = 60^\circ$ .

The values of the obtained results are summarized in Table 2. The error was computed with respect to the finest mesh. For example, the error for MVF was computed as  $err = 100 \times (MVF - MVF_{@N_m=5}) / MVF_{@N_m=5}$ . As seen, a mesh with  $N_m = 3$  or higher can compute MVF and stored energy with 0.5% error or less. Figure 5 depicts the time history of MVF for various mesh sizes, which agrees with the results of Table 2 over the melting process. Thus, as a fair trade between computational cost and accuracy, the mesh with  $N_m = 3$  was adopted for the computation of the results section.



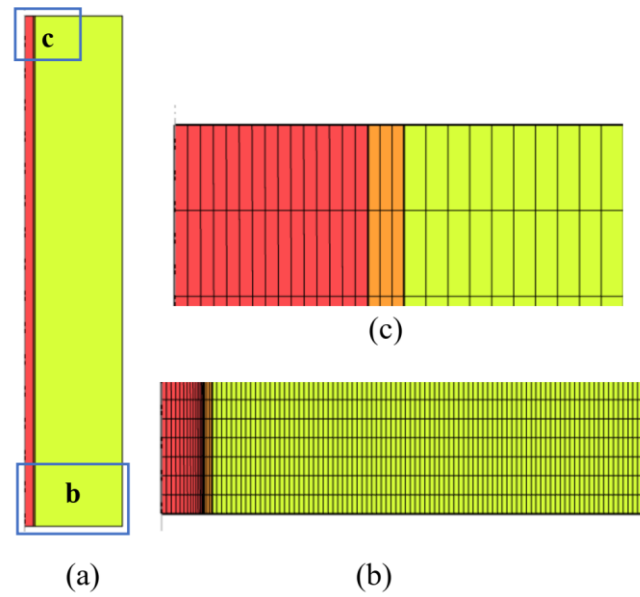


**Figure 4.** A view of the utilized mesh with  $N_m = 3$ . (a) An overall view of the geometry; (b) mesh at the bottom section of the LHTES; (c) mesh at the top next to the outlet. The mesh in the HTF region is non-uniform, with more density next to the tube wall.

**Table 2.** The computed characteristics for various mesh sizes at  $t = 4$  h when  $P_{in} = 5$  Pa,  $\zeta = 0.2$ , and  $\theta = 60^\circ$ . The computational time was reported for a full melting. A mesh with  $N_m \geq 3$  provides results with 0.5% error or smaller, which is acceptable for most engineering applications.

$N_m$	MVF	%err	$Q_{store}$ (kJ)	%err	Computational Time (min)
2	0.6958	1.6	1422.7	0.9	34
3	0.6883	0.5	1414.2	0.3	74
4	0.6860	0.1	1411.5	0.1	135
5	0.6851	0.0	1410.6	0.0	217

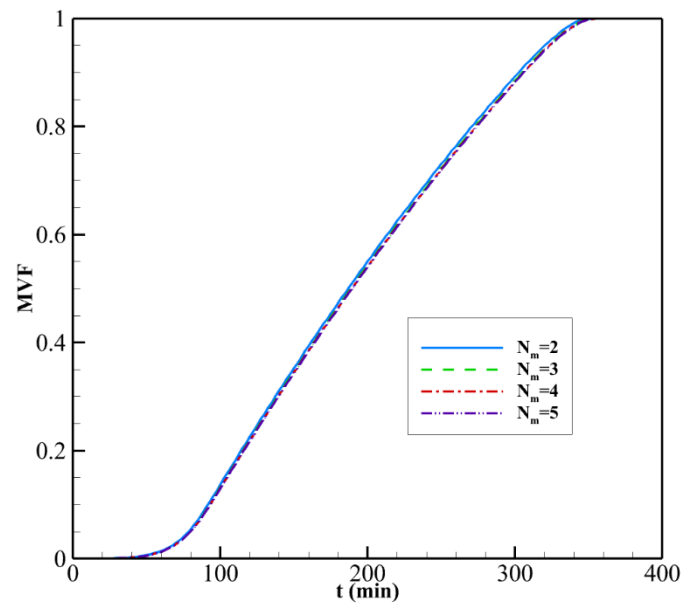


**Figure 5.** The time history of MVF for various mesh sizes when  $P_{in} = 5$  Pa,  $\zeta = 0.2$ , and  $\theta = 60^\circ$ . A mesh with  $N_m = 2$  slightly overpredicts the MVD, while there is no notable difference between predicted MVF for a mesh with size  $N_m \geq 3$  or higher. Thus, mesh with  $N_m = 3$  was adopted for simulations of the present study.

### 3.3. Model Verification

Zheng et al. [39] empirically examined the melting of paraffin wax in a square enclosure filled with copper metal foam. The paraffin in the enclosure was initially at a super cold temperature of 14 °C and fully solid. The enclosure's height and width were 100 mm. The left enclosure was heated by an electrical heater with a heat flux of 1150 W/m<sup>2</sup>. The PCM and MF in the enclosure absorb the heat, and the temperature increases gradually until the PCM reaches the melting temperature  $T_f = 55.3^\circ$ . Figure 6 illustrates a comparison between the simulated results of the present study and the observations of Zheng et al. [39]. The porosity was  $\varepsilon = 0.95$  with  $PPI = 5$  and  $\zeta = 0$ . The permeability and the effective thermal conductivity of metal foam ( $k_{MF, eff}$ ) were computed at  $8.3857 \times 10^{-7} \text{ m}^2$  and  $6.33 \text{ W}/(\text{m}\cdot\text{K})$ , respectively.

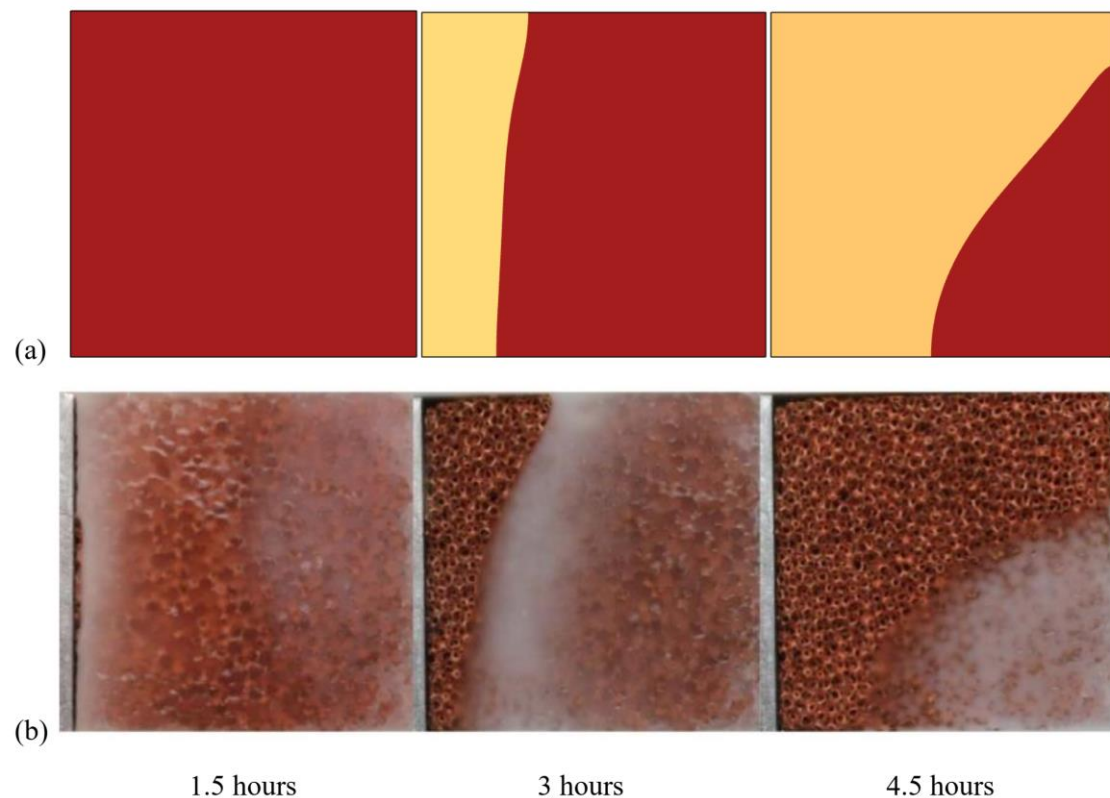


**Figure 6.** Heating of an enclosure filled by the copper metal foam of porosity 0.95. Verification of (a) the present simulations with (b) observations of Zhang et al. adapted with permission from Ref. [39]. 2018, Elsevier.

The temperatures were measured at the heated wall and over a vertical line with a 2.5 cm distance from the heated wall. Figure 7 illustrates a comparison between the time history of the measured ([39]) and computed (present study) temperatures. The simulations are computed for local thermal equilibrium (LTE) and LTNE models. LTE was obtained by considering a significant interaction between phases ( $h_v = 10^{12} \text{ W}/\text{m}^3$ ). The results show the LTNE is only significant near the heated wall while there is no significant difference between porous and PCM far from the wall. LTNE model provides a temperature prediction closer to experiments.

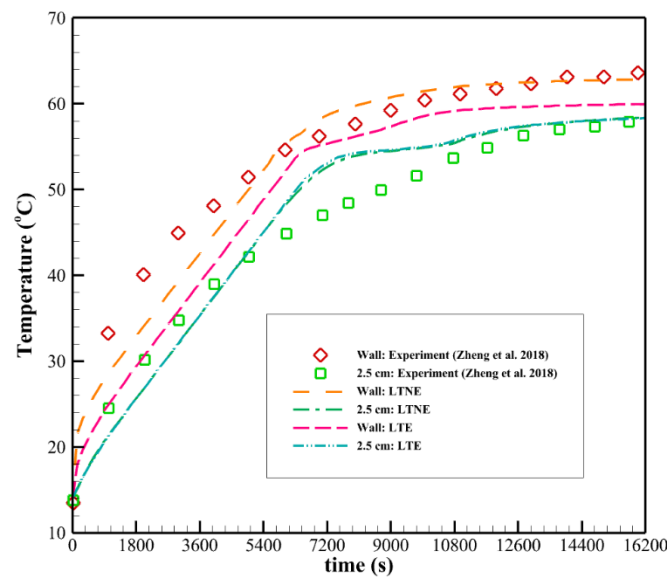


**Figure 7.** Time history of the temperature at the heated wall and over a vertical line with a 2.5 cm distance from the heated wall. The experimental results of [39] are plotted against the present simulation. The LTNE and LTE are reported. There is no significant difference between LTE and LTNE models far from the wall (2.5 cm). However, there is a notable difference between the two models next to the wall. The LTNE model predicts results with more agreement with the experimental observations.

As another comparison, the free convection heat transfer in an enclosure with the temperature difference between side walls was simulated. The enclosure was filled with an anisotropic porous medium [45]. In [45], the thermal conductivity was a function of the material space,  $k(x, y)$ , and it was introduced with a gradient in  $x$ - and  $y$ - directions depending on a distribution parameter,  $\zeta$ . Figure 8 compares the non-dimensional temperatures of the present computations and those of [45] when  $\zeta = 2.0$ . Figure 8 depicts the excellent proximity of the present computations and the literature results.

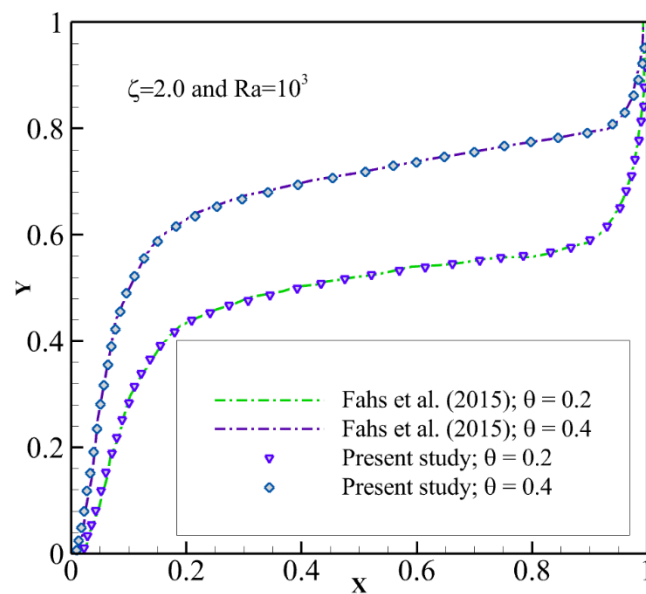


**Figure 8.** The obtained isotherms in [45] and the isotherms of the present simulations. The isotherms are in excellent agreement with the literature study for free convection in an anisotropic medium.

### 4. Results and Discussions

The impact of the MF anisotropic angle ( $\theta$ ) and the inlet pressure  $P_{in}$  were investigated on the charging time and the thermal behavior of the LHTES unit. As explained in the modeling section, the inlet temperature ( $T_h$ ) and anisotropic parameter ( $\zeta$ ) were kept constant. The anisotropic angle ( $\theta$ ) was addressed for  $-90^\circ, -75^\circ, -60^\circ, -45^\circ, -30^\circ, -15^\circ,$  and  $0^\circ$ , and positive values of these angles. The simulations were also performed for three inlet pressures ( $P_{in}$ ) of 5 Pa, 7.5 Pa, and 10 Pa. Moreover, three reference cases of  $\zeta = 0$  and  $P_{in} = 5, 7.5,$  and 10 Pa were investigated. The investigated cases are summarized in Table 3.

**Table 3.** Detail of simulated cases for various values of inlet pressure and anisotropic angles and reference cases when  $\zeta = 0.2$ .

Case	$\zeta$	$P_{in}$	$\theta$	Case	$\zeta$	$P_{in}$	$\theta$
1	0.2	5	-90	22	0.2	7.5	30
2	0.2	5	-75	23	0.2	7.5	45
3	0.2	5	-60	24	0.2	7.5	60
4	0.2	5	-45	25	0.2	7.5	75
5	0.2	5	-30	26	0.2	7.5	90
6	0.2	5	-15	27	0.2	10	-90
7	0.2	5	0	28	0.2	10	-75
8	0.2	5	15	29	0.2	10	-60
9	0.2	5	30	30	0.2	10	-45
10	0.2	5	45	31	0.2	10	-30
11	0.2	5	60	32	0.2	10	-15
12	0.2	5	75	33	0.2	10	0
13	0.2	5	90	34	0.2	10	15
14	0.2	7.5	-90	35	0.2	10	30
15	0.2	7.5	-75	36	0.2	10	45
16	0.2	7.5	-60	37	0.2	10	60
17	0.2	7.5	-45	38	0.2	10	75
18	0.2	7.5	-30	39	0.2	10	90
19	0.2	7.5	-15	40	0	5	0
20	0.2	7.5	0	41	0	7.5	0
21	0.2	7.5	15	42	0	10	0

Figure 9 depicts the MVF and stored energy over time for various anisotropic angles. As seen, the decrease in the anisotropic angle from  $90^\circ$  to  $0^\circ$  accelerates the melting process and reduces the melting time. The results for negative angles are very close to similar positive angles. This is since the difference between the positive and negative angles is just the minor difference produced by  $\sin(\theta)\cos(\theta)$  terms in the thermal conductivity and permeability matrixes. An isotropic case, a reference case with the average porosity and permeability, was also simulated, and the results were added to this figure. The results show that the typical isotropic MF (reference case) can produce a melting process between the anisotropic MF when the anisotropic angle is  $|\theta| > 45^\circ$ . However, the decline of the anisotropic angle below  $45^\circ$  down to  $0^\circ$  provides an accelerated melting process.

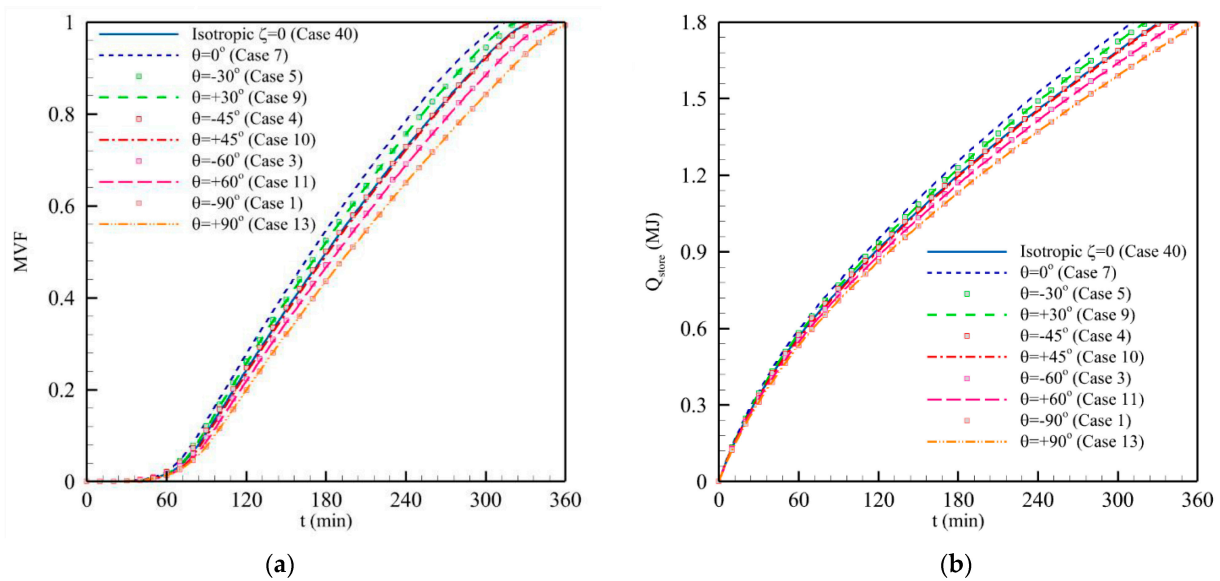


**Figure 9.** The impact of anisotropic angle ( $\theta$ ) on the MVF (a) and stored energy (b) over time when  $\zeta = 0.2$  and  $P_{in} = 5$  kPa.

In practice, reaching different anisotropic angles is easy since it can change by the mounting-direction of the anisotropic MF in an enclosure. The reason for the improvement of melting heat transfer by the increase in anisotropic angle is attributed to the conductivity matrix. Using Equation (2), the thermal conductivity and permeability matrix can be obtained as follows for  $\theta = 0^\circ$  and  $\theta = 90^\circ$ :

$$\begin{aligned}
 k_{\text{eff,MF}} &= \begin{bmatrix} k_1 & 0 \\ 0 & k_2 \end{bmatrix} \quad \text{and} \quad \kappa = \begin{bmatrix} \kappa_1 & 0 \\ 0 & \kappa_2 \end{bmatrix} \quad \text{when } \theta = 0^\circ \\
 k_{\text{eff,MF}} &= \begin{bmatrix} k_2 & 0 \\ 0 & k_1 \end{bmatrix} \quad \text{and} \quad \kappa = \begin{bmatrix} \kappa_2 & 0 \\ 0 & \kappa_1 \end{bmatrix} \quad \text{when } \theta = 90^\circ
 \end{aligned}
 \tag{24}$$

where  $k_1 > k_2$  and  $\kappa_1 < \kappa_2$ . Thus, for a case with  $\theta = 0^\circ$ , there is a better thermal conductivity in the  $r$  direction to transfer the heat from the HTF tube wall into the enclosure. Moreover, there would be a high permeability in the  $z$ -direction, allowing the molten liquid to move in an upward direction and disperse the heat by the advection mechanism. In contrast, a case with  $\theta = 90^\circ$  provides minimal thermal conductivity in the  $r$ -direction and minimal permeability in the  $z$ -direction, which declines the advection and conduction mechanisms in the molten PCM. The same conclusion is proper for negative angles.

The stored energy shows the same trend as MVF since the thermal energy storage is dominated by latent heat energy storage. The sensible energy is also most significant in the liquid region, closely following the MVF. Thus, the highest energy storage rate can be seen for an anisotropic angle  $\theta = 0^\circ$ .

Figure 10 shows the temperature distribution and the interface for phase change heat transfer in the unit when the anisotropic angle is  $0^\circ$ . The temperature distribution is reported for the PCM ( $T_{\text{PCM}}$ ) and MF ( $T_{\text{MF}}$ ) phases. The temperature labels have not been added to avoid congestion. The contour levels are  $2^\circ$ , and the minimum and maximum temperature of each image were also reported above the image. The time of each image is also indicated below the image. As seen, the temperature differences between MF and PCM phases are not much. The differences are mostly next to the insulated wall. There is no temperature difference at the HTF tube wall, indicating accurate implementation of the continuity of temperatures at the boundary. The difference between the PCM and MF at the insulated wall is due to MF's superior thermal conductivity, which better channels the heat into the solid regions. There are also slight temperature differences at the bottom

due to the natural convection effects. They are significant at the final times, with a notable amount of liquid PCM and convection circulation flows.

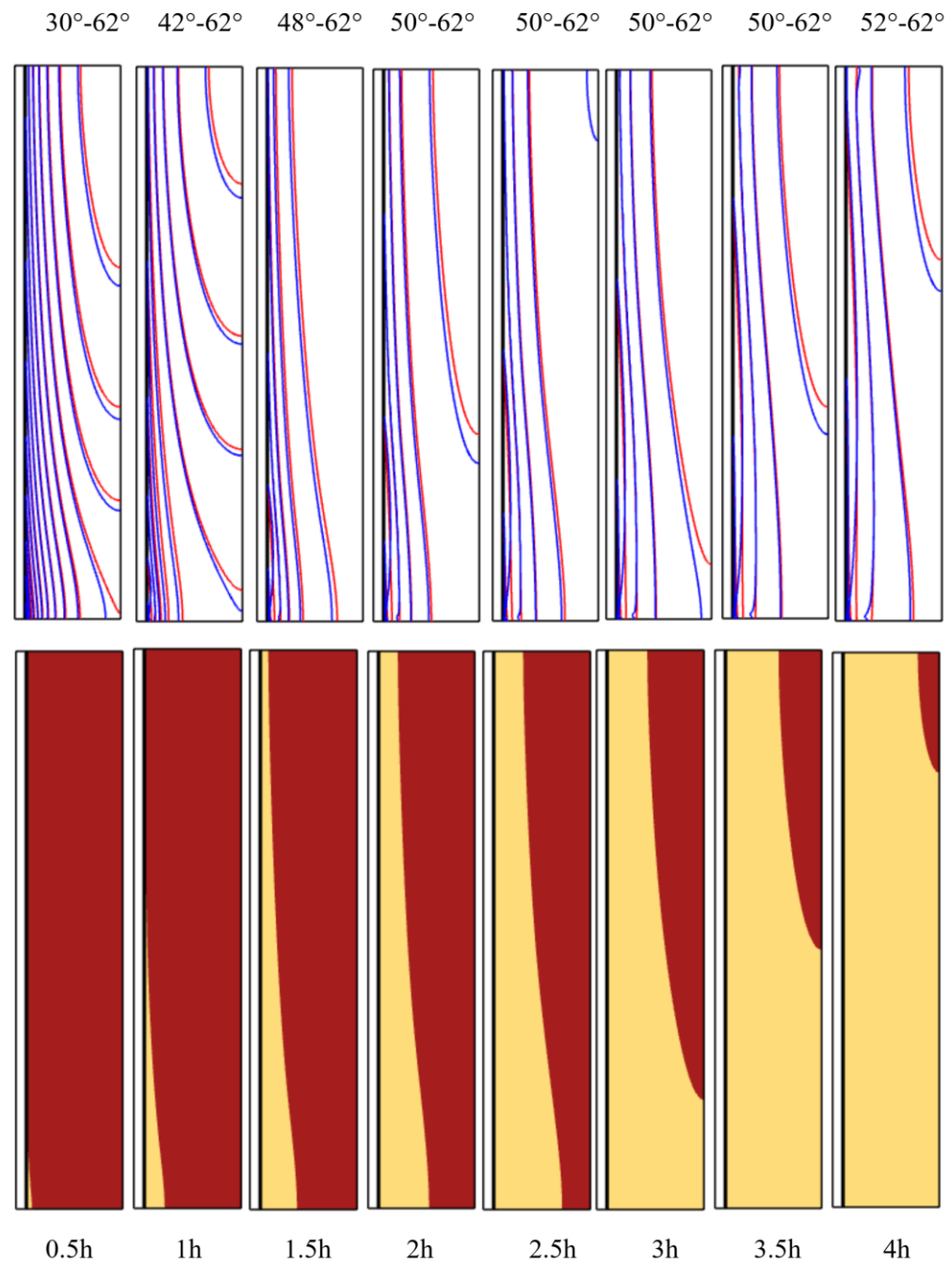


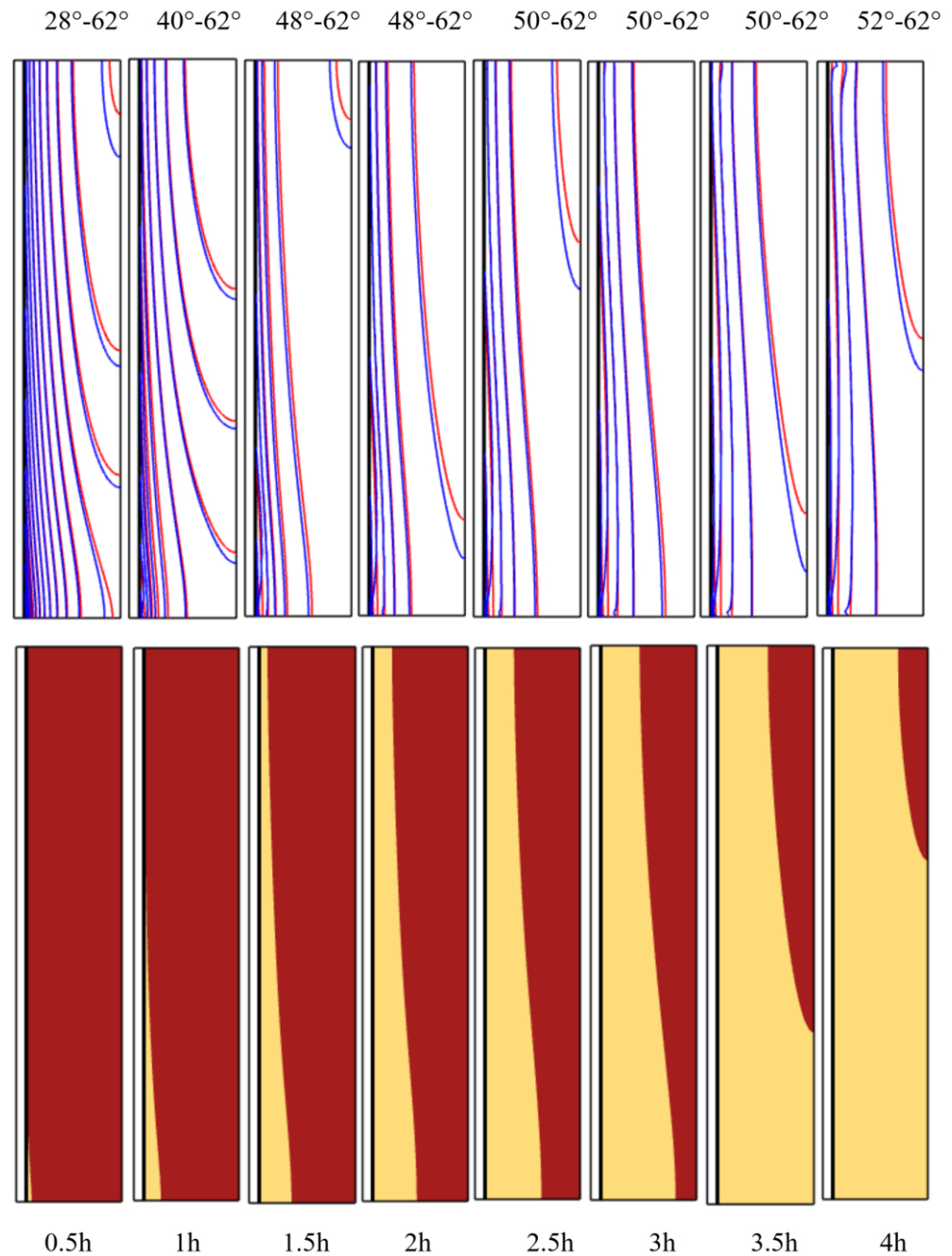
**Figure 10.** The unit’s temperature distribution (first row) and melting interface (second row) when  $P_{in} = 5$  kPa,  $\zeta = 0.2$ , and  $\theta = 0^\circ$ . The red and blue lines denote the temperature in MF and PCM, respectively. The contour levels are  $2^\circ$ , and the range of temperatures is written above each plot.

The melting interface starts from the bottom, where the HTF enters the tube at the highest average temperature. Moreover, the convection heat transfer between the HTF flow and tube wall is highest in the entrance region. The heat reaches the PCM, and melting commences. Thus, the melting front develops from the bottom and extends toward the top right. Due to the presence of MF in the unit, the natural convection circulation is weak, and the melting front mainly progresses from the bottom.

Figure 11 shows the isotherms and melting front for an isotropic case with no anisotropic properties. The temperature difference between  $T_{PCM}$  and  $T_{MF}$  is almost similar to the

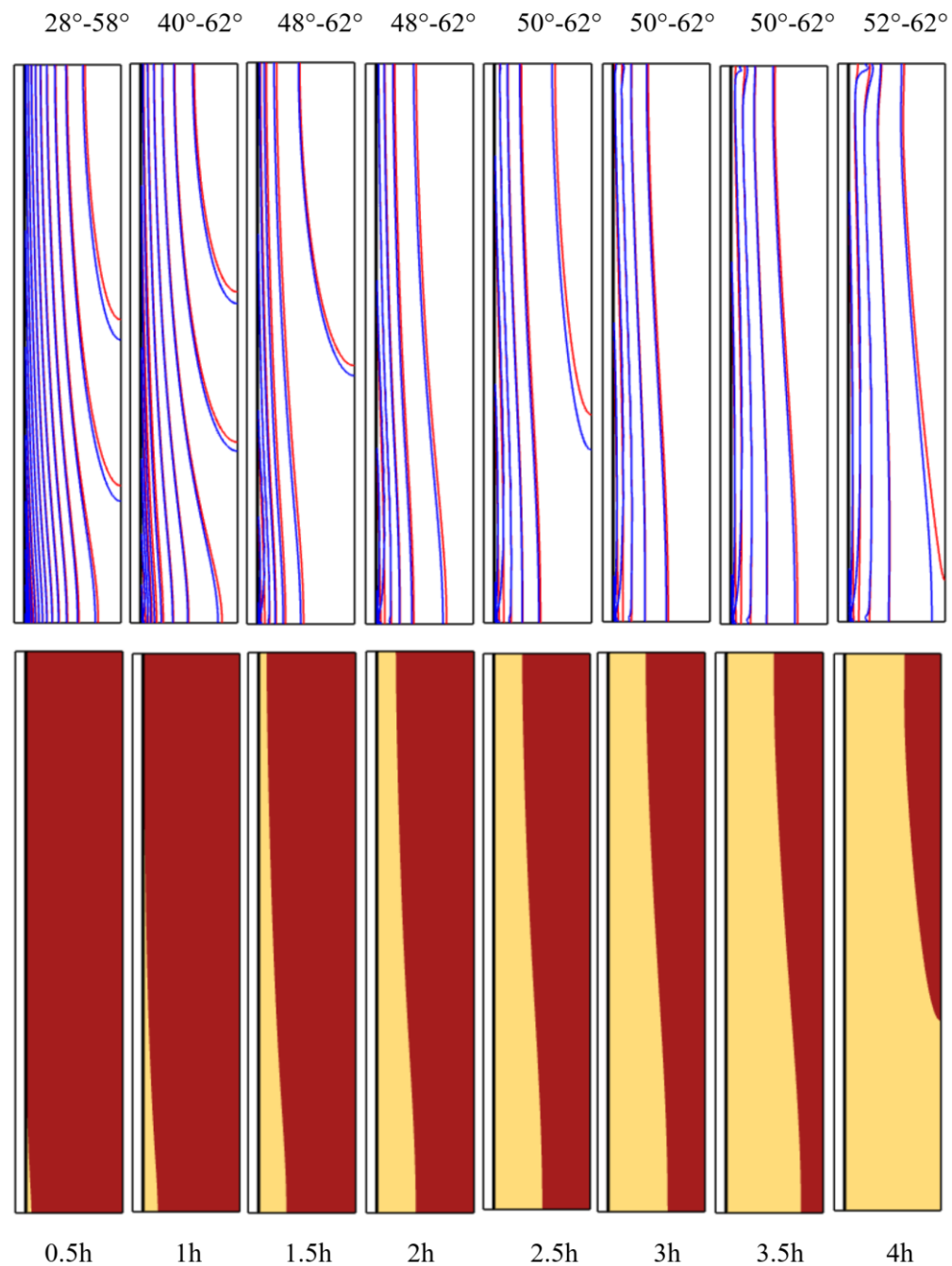


anisotropic case of  $\theta = 0^\circ$ , which was addressed in Figure 10. The difference between isotherm lines near the bottom is more pronounced. The MVF maps also show that the interface moves toward the top right of the enclosure more slowly compared to the anisotropic case of  $\theta = 0^\circ$ . A comparison between the melting interface of Figures 10 and 11 at  $t = 4$  h reveals a more solid area for the isotropic case (Figure 11).



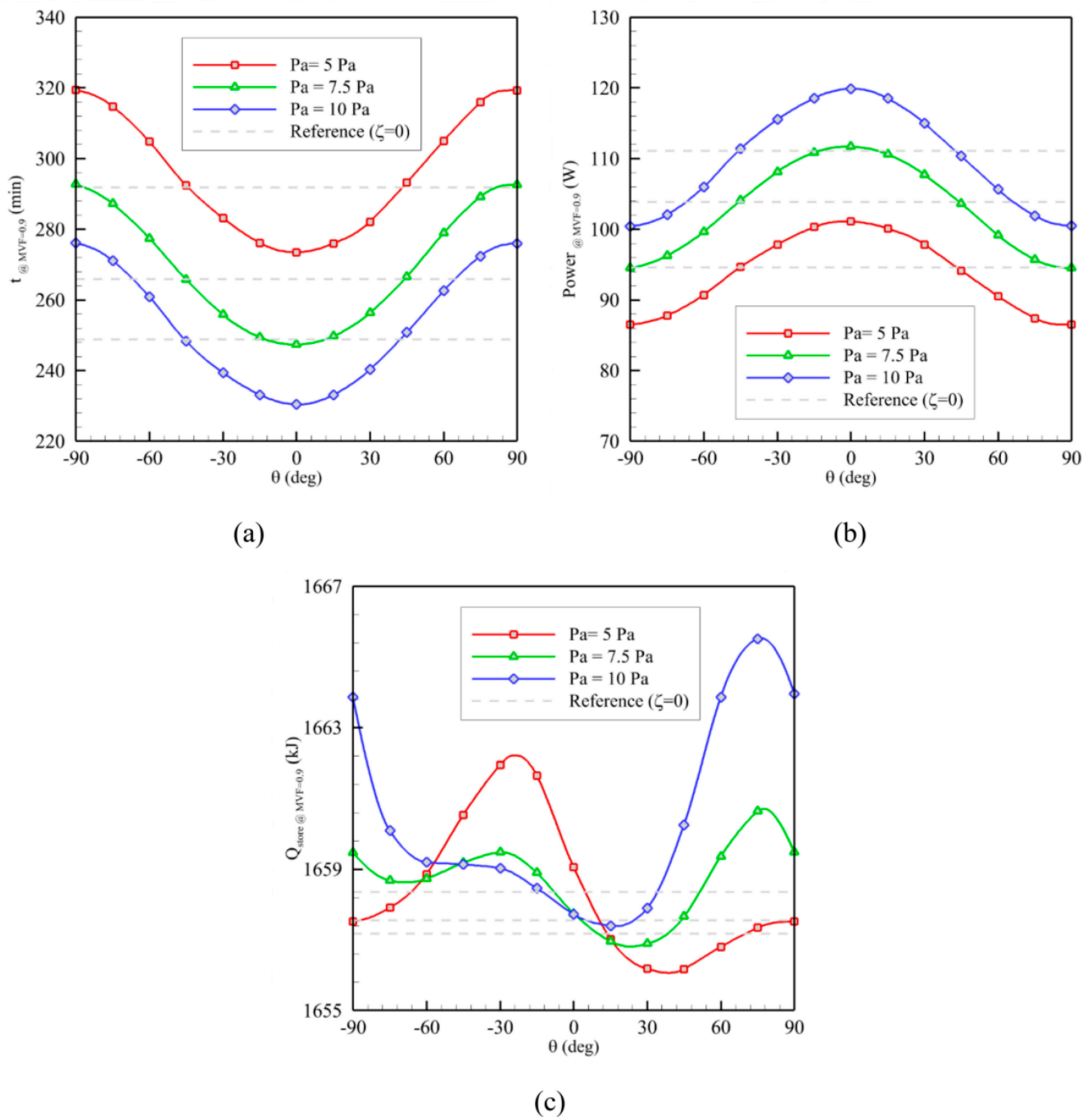
**Figure 11.** The temperature distribution (first row) and melting interface (second row) in the unit when  $P_{in} = 5$  kPa and  $\zeta = 0$  with no anisotropic angle. The red and blue lines denote the temperature in MF and PCM, respectively. The contour levels are  $2^\circ$ , and the range of temperatures is written above each plot.

Figure 12 shows the temperature and melting maps for an isotropic case with  $\theta = 90^\circ$ . The difference between  $T_{PCM}$  and  $T_{MF}$  lines is almost similar to previous images. However, the difference is more inclined to the vertical direction, where the thermal conductivity of MF is slightly higher in a vertical direction for this case.



**Figure 12.** The unit’s temperature distribution (first row) and melting interface (second row) when  $P_{in} = 5$  kPa,  $\zeta = 0.2$ , and  $\theta = 90^\circ$ . The red and blue lines denote the temperature in MF and PCM, respectively. The contour levels are  $2^\circ$ , and the range of temperatures is written above each plot.

Figure 13 plots the impact of anisotropic angle ( $\theta$ ) and inlet pressure ( $P_{in}$ ) on the MVF, energy storage power, and stored energy when the melting fraction reaches 0.9. The value of  $MVF = 0.9$  was selected for analysis since, at this number, most of the enclosure is in a liquid state, representing the unit’s thermal behavior next to a full charge level. When the enclosure reaches a fully charged level ( $MVF = 0.999$ ), there is no solid PCM left, and the unit behavior is mainly dominated by a small variation of sensible heat. Thus, an appropriate state next to the fully charged state, i.e.,  $MVF = 0.9$ , was adopted to investigate the impact of control parameters on the thermal behavior of the unit.



**Figure 13.** The heat transfer characteristics as a function of anisotropic angle ( $\theta$ ) and HTF inlet pressure ( $P_{in}$ ). (a): The melting time was computed when MVF = 0.90, noted as  $t_{@MVF=0.9}$ . (b): Energy storage power at MVF = 0.9, indicated by  $Power_{@MVF=0.9}$ . (c): The stored energy when MVF = 0.9, denoted by  $Q_{store@MVF=0.9}$ .

Figure 13a shows that the increase in inlet pressure notably reduces the charging time. Regardless of the inlet pressure, the charging time is minimal for an anisotropic angle  $\theta = 0^\circ$ . This finding agrees with the findings of Figure 9 for a fully melted unit when  $P_{in} = 5$  Pa. For the optimum anisotropic angle  $\theta = 0^\circ$ , increasing the inlet pressure from 5 Pa to 7.5 Pa (a 50% increase) reduces the melting time from 273 min to 247 min. Thus a 50% increase in the inlet pressure could save the charging time by 9.5%. For an inlet pressure of 10 Pa, the optimum melting time was 230 (min), which is only 15.7% lower than that of  $P_{in} = 5$  Pa.

The Reynolds number for the inlet pressures of 5 Pa, 7.5 Pa, and 10 Pa was 1054, 1628, and 2233, respectively.

Moreover, a semi-symmetric behavior for negative and positive angles can be observed. The maximum charging time corresponds to anisotropic angles  $+90^\circ$  and  $-90^\circ$ . These trends agree with the results of Figure 9 for a fully charged enclosure.

The energy storage power (Figure 13b) shows a similar trend of behavior to the charging time but in reverse. Figure 13c shows the amount of stored energy. There are small energy fluctuations ( $<1\%$ ) for various inlet pressure and anisotropic angles when the enclosure reaches a charging state with  $MVF = 90\%$ . These fluctuations are primarily due to the sensible heat energy, a function of the unit's local temperature distribution. Most of the enclosure is in a liquid state, with slight temperature variations in the liquid phase. Thus, since there are slight variations in the amount of stored energy, the behavior of the energy storage power is almost proportional to the inverse of melting time (Figure 13b). The maximum energy storage power for the unit is 119.9 W, obtained for  $P_{in} = 10$  Pa and  $\theta = 0^\circ$ . The reference lines for an enclosure filled by an isotropic metal foam are also plotted in all sub-figures of Figure 13. Figure 13a,b show that an anisotropic angle below  $45^\circ$  ( $|\theta| < 45^\circ$ ) could reduce the melting time and increase the charging power compared to an isotropic metal foam design.

The charging time ( $MVF = 0.9$ ) for the isotropic metal foam was computed as 292 min, 266 min, and 249 min for inlet pressures of 5 Pa, 7.5 Pa, and 10 Pa. An optimum anisotropic design ( $\theta = 0^\circ$ ) could reduce the charging time to 273 min (6.5%), 247 min (7.1%), and 230 min (7.6%). Considering all inlet pressures, the improvements average is about 7%. The same improvement can be seen for energy storage power. Thus, compared to an isotropic metal foam design, an anisotropic property ( $\zeta = 0.2$ ) could improve the unit's thermal performance by about 7% without impacting the unit's thermal energy storage capacity or adding weight.

## 5. Artificial Intelligence and Optimization

A neural network (NN) is a set of algorithms that attempt to discover fundamental relationships in a group of data through a process that mimics how the human brain works. Thus, a NN can be explained as a system of organic or artificial neurons. A "neuron" in a NN is a function introduced mathematically, which renders information following its specific architecture. Thus, such NN is analogous to statistical methods such as regression and curve fitting [46]. Since the neurons in a mathematical neural network are introduced artificially, the resulting network is an Artificial Neural Network (ANN).

NNs are capable of adapting to variable inputs and thus providing accurate outputs. A NN contains layers of interconnected nodes (perceptron) and activation functions. A feed-forward neural network, which was utilized in the present study, sends information in one direction through its entry node and processes them in a unidirectional fashion until they reach the output node [46].

The computational time for each simulation was reported in Table 2. It was observed that the computational time for the numerical experiments was more than one hour. This means, each simulation for a set of the design parameters, i.e.,  $P_{in}$  and  $\theta$ , takes more than an hour. Therefore, finding an accurate numerical relationship between the design parameters and the melting behavior ( $MVF$ ) was computationally expensive. Here, the ANN is used to find an accurate map between the design parameters and the design target at a low cost.

In order to train the ANN, the melting process data for cases 1–39, consisting of 4998 sample data, were fed to a neural network to learn the relationship between the input control variables of inlet pressure ( $P_{in}$ ), anisotropic angle ( $\theta$ ), and melting time ( $t$ ), and the target data ( $MVF$ ). The melting instances were captured from simulation data at each 2.5 min instance until a full melting reaches. Then, the ANN was trained and used to learn the relationship between the input and target data. The size of the training database was 4998 samples which were divided into 70% training, 15% test, and 15% validation. Table 4 shows the list of input and output variables.

**Table 4.** A summary of the input and output variables for the ANN model and the data partitions.

Input Variables			Output Variable	Train	Test	Validation
$P_{in}$ (Pa)	$\theta$ (deg)	$t$ (s)	MVF	70%	15%	15%

The Levenberg–Marquardt optimization, which is a network training function that updates weight and bias values, was used. This method is one of the fastest supervised algorithms, which uses the backpropagation algorithms for training. Training record (epoch and performance) returned as a struct whose fields depend on the network training function. A trained neural network structure contains the following parts: (1) Training, data splitting, and performance functions and parameters; (2) Data split index for training, validation, and test sets; (3) Data split mask for training validation and test sets; (4) Number of epochs and best epoch; (5) A list of training state names (states); (6) A field for each state name that records the value during training; and (7) Best network performance such as train, validation, test and best.

Some studies, such as [47,48], utilized systematic a hyper-parameter method to select the ANN details. However, in the present study, some preliminary investigations on the number of neurons and the number of hidden layers were performed manually. It was noted that using two hidden layers with many neurons results in excellent training data, but results in an overfit and deteriorates the validation predictions. Thus, only ten neurons with a single hidden layer were used to avoid overfitting issues. Since the utilized neural network was fairly simple and could well predict the physical model no further investigations were seen necessary for fine-tuning the ANN parameters.

Figure 14 shows the structure of the utilized neural network, which consists of ten neurons in its first hidden layer and an output layer made of one neuron. Figure 15 depicts the neural network prediction accuracy for the test, training, and validation aspects. It should be noted that the validation data should not be just used for validation [49] and not be fed to the ANN during the training or other processes. Here, the validation data were independent of the training process, but it was just plotted in the same figure for sake of representation. As seen, the ANN learns to predict the results after a few epochs very well. The validation process consists of results for cases that the ANN has never seen during the training and test process. Thus, this index can show the reliability of the ANN in estimating the solution field. The best validation was achieved after 58 epochs; hence, this state was adopted as the best state of ANN for producing the maps of MVF as a function of control parameters. Figure 16 contains the subplots for the train, test, and validation data details. The  $y$ -axis shows the normalized estimated output while the  $x$ -axis shows the amount of normalized target (CFD) value for each sample. This figure shows that the ANN estimated most of the data with excellent accuracy.

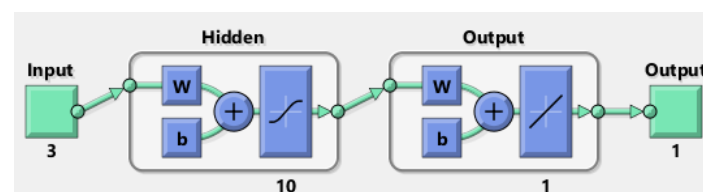


**Figure 14.** The structure of the utilized neural network. The input layer receives three control parameters of time ( $t$ ), inlet pressure ( $P_{in}$ ), and anisotropic angle  $\theta$  and passes them to a fully connected hidden layer of ten neurons. Then, there is the output layer which provides the corresponding MVF.

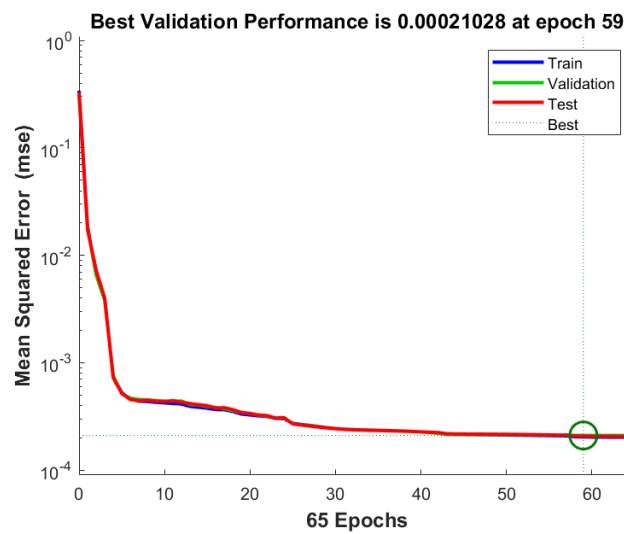


Figure 15. The validation performance of the ANN during the training process. The best performance was obtained after 58 epochs. After 58 epochs, the validation accuracy slightly increases, indicating potential overfit. Thus, the network at 58 epochs was used as the best-trained network.

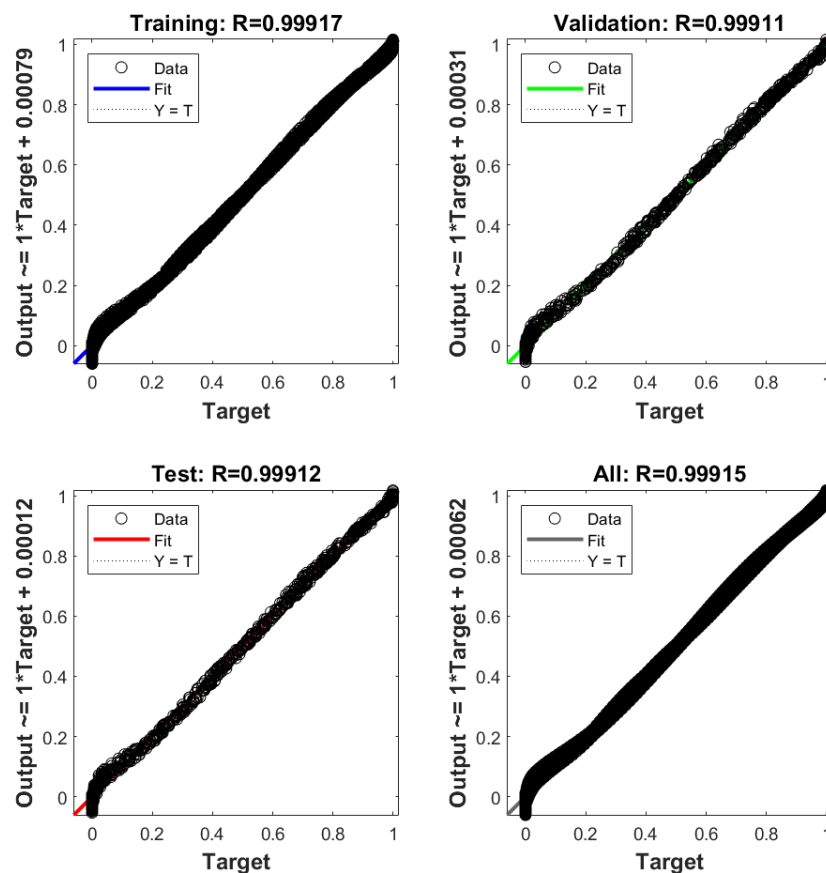
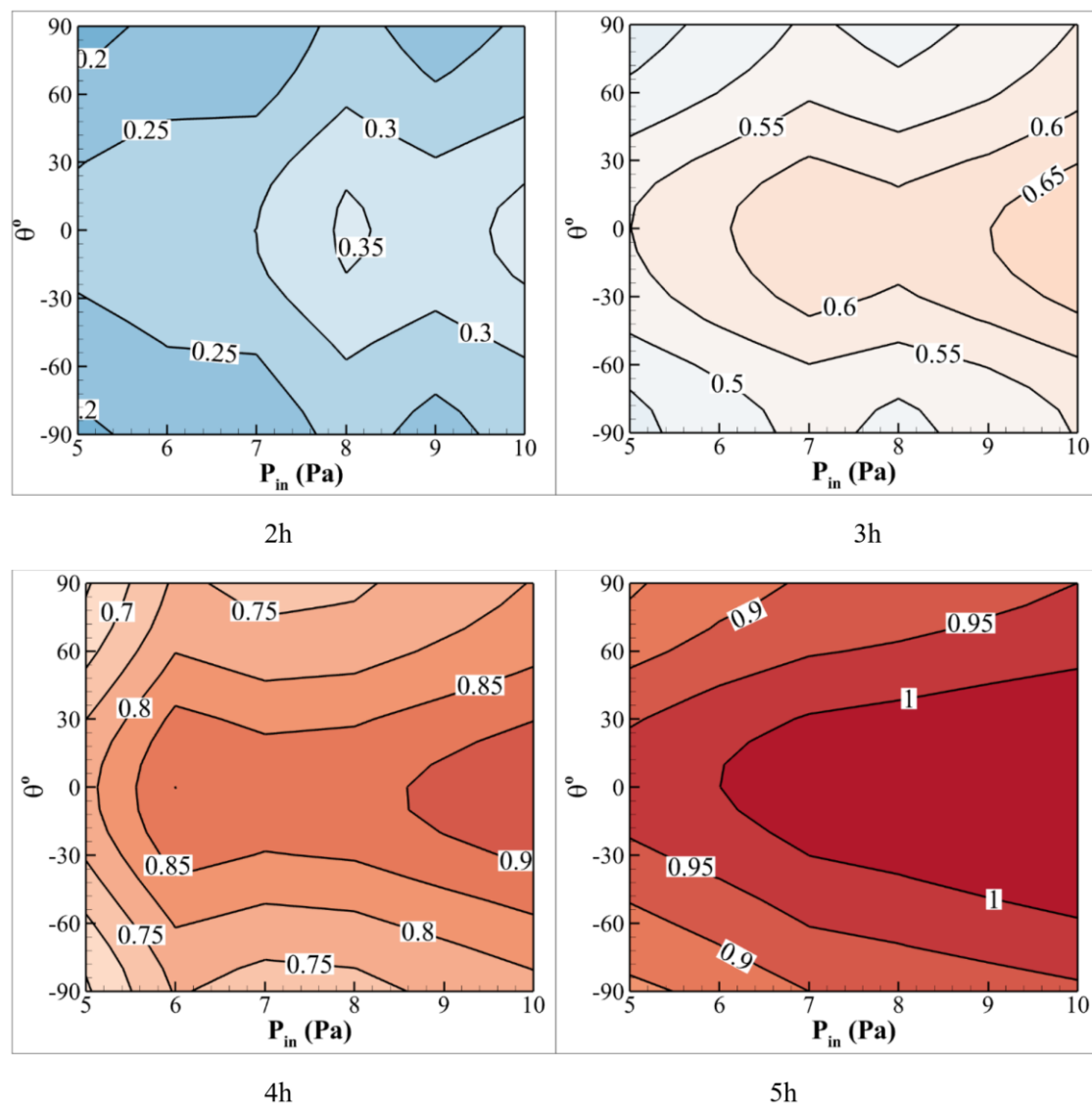


Figure 16. The regression performance of the trained ANN (at 58 epochs) for the training, test, and validation data. All of the plots show an R-value higher than 0.99, which shows the excellent performance of the ANN in learning the transient behavior of MVF in the shell-tube thermal energy storage unit.

The trained ANN was used to produce maps of MVF as a function of control parameters. Figure 17 depicts the contours of MVF for various anisotropic angles and inlet pressures. The MVF was simulated using the trained ANN. The inlet pressure was adopted



in the range of 5 Pa–10 Pa with intervals of 1 Pa, while the anisotropic angle was in the range of  $-90^\circ$  to  $+90^\circ$  with an interval of  $10^\circ$ . The plots were created for hourly melting intervals of 2 to 5 h. Based on the previous data, an anisotropic angle of  $45^\circ$  provides similar data to a uniform metal foam with no anisotropic properties. A zero anisotropic angle can provide the melting volume fraction at a low inlet pressure comparable with a much higher inlet pressure but with anisotropic angles about  $45^\circ$  or higher. Thus, an optimum anisotropic angle can promote MVF without adding weight to an LHTES unit.



**Figure 17.** The impact of inlet pressure and anisotropic angle on the MVF at different time snaps. The contours are generated using the trained neural network with a validation R-value larger than 0.999. The results are reported for four time-snaps of 2, 3, 4, and 5 h. After 2 h of heating, the enclosure is mainly filled with 0.25–0.35 liquid. The liquid fraction raises to the ranges of 0.55–0.65, 0.7–0.9, and 0.9–1.0 for 3, 4, and 5 h of hearing, respectively. In all maps, the maximum inlet pressure and a zero anisotropic angle ( $\theta = 0^\circ$ ) provide the highest MVF. The increase in anisotropic angle reduces the MVF.

## 6. Conclusions

The impact of utilizing an anisotropic metal foam on the melting behavior of a PCM was addressed in a shell-tube latent heat storage unit. The permeability and thermal conductivity were a function of anisotropic intensity and angle. A two-equation heat transfer

model, based on the local thermal non-equilibrium approach LTNE model, was employed to capture the metal foam and PCM temperatures. About 40 numerical experiments were executed, and the impact of the anisotropy angle (between  $-90^\circ$  and  $90^\circ$  with an anisotropy factor  $\zeta = 0.2$ ) and the HTF inlet pressures on the melting behavior were examined. Results are compared to a reference case of isotropic permeability and conductivity. An artificial neural network was utilized to learn the transient behavior of the melting heat transfer in the LHTES unit. Then, the neural network model was used to discuss the critical impact of control parameters on the melting rate.

Results showed a decrease in the anisotropy angle from  $|\theta| = 90^\circ$  to  $0^\circ$  accelerates the melting rate. Nevertheless, the typical isotropic MF (reference case) can produce a melting process between the anisotropic MF when the anisotropic angle is  $|\theta| = 45^\circ$ . However, increasing the anisotropic angle above  $45^\circ$  to  $90^\circ$  slows the melting process.

The increase in the inlet pressure of the HTF from 5 Pa to 10 Pa accelerates the melting process by about 16% for the optimum angle of anisotropy  $\theta = 0^\circ$  and increases the storage capacity. Hence the maximum storage power is achieved for  $\theta = 0^\circ$  and  $P_{in} = 10$  Pa.

The feed-forward neural network successfully learned the transient behavior of MVF from 4998 sample data with an R-value greater than 0.99. Using the ANN, hourly maps of MVF as a function of pressure and anisotropic angles were produced. Using the MVF maps, the advantage of anisotropic angle versus pressure drop was discussed. During the whole melting process, using a zero-angle anisotropic MF could significantly accelerate the melting process compared to a uniform MF.

**Author Contributions:** Conceptualization, J.S., M.G. (Mehdi Ghalambaz), M.G. (Mohammad Ghalambaz), M.F. and M.I.; methodology, J.S., M.G. (Mehdi Ghalambaz), M.I., M.G. (Mohammad Ghalambaz) and M.F.; software, M.G. (Mehdi Ghalambaz), M.G. (Mehdi Ghalambaz), M.F. and J.S.; validation, M.G. (Mehdi Ghalambaz) and M.G. (Mohammad Ghalambaz), formal analysis, M.G. (Mehdi Ghalambaz), M.G. (Mohammad Ghalambaz), M.F. and J.S.; investigation, M.G. (Mehdi Ghalambaz), M.G. (Mohammad Ghalambaz) and M.F.; resources, M.G. (Mohammad Ghalambaz), M.F. and J.S.; data curation, J.S.; writing—original draft preparation, J.S., M.G. (Mehdi Ghalambaz), M.F., M.I. and M.G. (Mohammad Ghalambaz); writing—review and editing, J.S., M.G. (Mehdi Ghalambaz), M.F., M.I. and M.G. (Mohammad Ghalambaz); visualization, M.G. (Mehdi Ghalambaz), M.F. and J.S.; supervision, M.G. (Mohammad Ghalambaz); project administration, M.G. (Mohammad Ghalambaz); funding acquisition, M.F. All authors have read and agreed to the published version of the manuscript.

**Funding:** This research was funded by Deanship of Scientific Research at Umm Al-Qura University for supporting this work by Grant Code: (22UQU4310414DSR02).

**Informed Consent Statement:** Not applicable.

**Data Availability Statement:** All data are reported in the text.

**Acknowledgments:** The authors would like to thank the Deanship of Scientific Research at Umm Al-Qura University for supporting this work by Grant Code: (22UQU4310414DSR02).

**Conflicts of Interest:** The authors declare no conflict of interest.

## References

1. Jouhara, H.; Żabnieńska-Góra, A.; Khordehgah, N.; Ahmad, D.; Lipinski, T. Latent thermal energy storage technologies and applications: A review. *Int. J. Thermofluids* **2020**, *5*, 100039. [[CrossRef](#)]
2. Li, Z.; Lu, Y.; Huang, R.; Chang, J.; Yu, X.; Jiang, R.; Yu, X.; Roskilly, A.P. Applications and technological challenges for heat recovery, storage and utilisation with latent thermal energy storage. *Appl. Energy* **2021**, *283*, 116277. [[CrossRef](#)]
3. Hassan, F.; Jamil, F.; Hussain, A.; Ali, H.M.; Janjua, M.M.; Khushnood, S.; Farhan, M.; Altaf, K.; Said, Z.; Li, C. Recent advancements in latent heat phase change materials and their applications for thermal energy storage and buildings: A state of the art review. *Sustain. Energy Technol. Assess.* **2022**, *49*, 101646. [[CrossRef](#)]
4. Bondareva, N.S.; Sheremet, M.A. Heat transfer performance in a concrete block containing a phase change material for thermal comfort in buildings. *Energy Build.* **2022**, *256*, 111715. [[CrossRef](#)]
5. Liu, W.; Bie, Y.; Xu, T.; Cichon, A.; Królczyk, G.; Li, Z. Heat transfer enhancement of latent heat thermal energy storage in solar heating system: A state-of-the-art review. *J. Energy Storage* **2022**, *46*, 103727. [[CrossRef](#)]

6. Sharma, A.; Pitchumani, R.; Chauhan, R. Solar air heating systems with latent heat storage-A review of state-of-the-art. *J. Energy Storage* **2022**, *48*, 104013. [CrossRef]
7. Srinivasan, G.; Rabha, D.; Muthukumar, P. A review on solar dryers integrated with thermal energy storage units for drying agricultural and food products. *Sol. Energy* **2021**, *229*, 22–38. [CrossRef]
8. Agrawal, A.; Rakshit, D. Review on thermal performance enhancement techniques of latent heat thermal energy storage (LHTES) system for solar and waste heat recovery applications. In *New Research Directions in Solar Energy Technologies*; Springer: Singapore, 2021; pp. 411–438.
9. Ghosh, D.; Ghose, J.; Datta, P.; Kumari, P.; Paul, S. Strategies for phase change material application in latent heat thermal energy storage enhancement: Status and prospect. *J. Energy Storage* **2022**, *53*, 105179. [CrossRef]
10. Mahdi, J.M.; Najim, F.T.; Aljubury, I.M.; Mohammed, H.I.; Khedher, N.B.; Alshammari, N.K.; Cairns, A.; Talebizadehsardari, P. Intensifying the thermal response of PCM via fin-assisted foam strips in the shell-and-tube heat storage system. *J. Energy Storage* **2022**, *45*, 103733. [CrossRef]
11. Tiari, S.; Hockins, A.; Shank, K. Experimental study of a latent heat thermal energy storage system assisted by varying annular fins. *J. Energy Storage* **2022**, *55*, 105603. [CrossRef]
12. Tiari, S.; Hockins, A.; Mahdavi, M. Numerical study of a latent heat thermal energy storage system enhanced by varying fin configurations. *Case Stud. Therm. Eng.* **2021**, *25*, 100999. [CrossRef]
13. Eisapour, A.H.; Shafaghat, A.; Mohammed, H.I.; Eisapour, M.; Talebizadehsardari, P.; Brambilla, A.; Fung, A.S. A new design to enhance the conductive and convective heat transfer of latent heat thermal energy storage units. *Appl. Therm. Eng.* **2022**, *215*, 118955. [CrossRef]
14. Laouer, A.; Teggat, M.; Tunçbilek, E.; Arıcı, M.; Hachani, L.; Ismail, K.A. Melting of hybrid nano-enhanced phase change material in an inclined finned rectangular cavity for cold energy storage. *J. Energy Storage* **2022**, *50*, 104185. [CrossRef]
15. Iachachene, F.; Haddad, Z.; Abu-Nada, E.; Sheremet, M.A. Natural convection melting of phase change material in corrugated porous cavities. *Sustain. Energy Technol. Assess.* **2022**, *53*, 102734. [CrossRef]
16. Mahdi, J.M.; Mohammed, H.I.; Talebizadehsardari, P.; Ghalambaz, M.; Majidi, H.S.; Yaïci, W.; Giddings, D. Simultaneous and consecutive charging and discharging of a PCM-based domestic air heater with metal foam. *Appl. Therm. Eng.* **2021**, *197*, 117408. [CrossRef]
17. Khademi, A.; Shank, K.; Mehrjardi, S.A.A.; Tiari, S.; Sorrentino, G.; Said, Z.; Chamkha, A.J.; Ushak, S. A brief review on different hybrid methods of enhancement within latent heat storage systems. *J. Energy Storage* **2022**, *54*, 105362. [CrossRef]
18. Cui, W.; Si, T.; Li, X.; Li, X.; Lu, L.; Ma, T.; Wang, Q. Heat transfer enhancement of phase change materials embedded with metal foam for thermal energy storage: A review. *Renew. Sustain. Energy Rev.* **2022**, *169*, 112912. [CrossRef]
19. Zhang, S.; Pu, L.; Mancin, S.; Dai, M.; Xu, L. Role of partial and gradient filling strategies of copper foam on latent thermal energy storage: An experimental study. *Energy* **2022**, *255*, 124517. [CrossRef]
20. Buonomo, B.; Manca, O.; Nardini, S.; Plomitallo, R.E. Numerical study on latent heat thermal energy storage system with PCM partially filled with aluminum foam in local thermal equilibrium. *Renew. Energy* **2022**, *195*, 1368–1380. [CrossRef]
21. Ge, R.; Li, Q.; Li, C.; Liu, Q. Evaluation of different melting performance enhancement structures in a shell-and-tube latent heat thermal energy storage system. *Renew. Energy* **2022**, *187*, 829–843. [CrossRef]
22. Zadeh, S.M.H.; Ghodrati, M.; Ayoubloo, K.A.; Sedaghatzadeh, N.; Taylor, R.A. Partial charging/discharging of bio-based latent heat energy storage enhanced with metal foam sheets. *Int. Commun. Heat Mass Transf.* **2022**, *130*, 105757. [CrossRef]
23. Bamdezh, M.A.; Molaieimanesh, G.R.; Zanganeh, S. Role of foam anisotropy used in the phase-change composite material for the hybrid thermal management system of lithium-ion battery. *J. Energy Storage* **2020**, *32*, 101778. [CrossRef]
24. Yu, P.; Wang, Y.; Ji, R.; Wang, H.; Bai, J. Pore-scale numerical study of flow characteristics in anisotropic metal foam with actual skeleton structure. *Int. Commun. Heat Mass Transf.* **2021**, *126*, 105401. [CrossRef]
25. Ren, Q.; Wang, Z.; Lai, T.; Zhang, J.F.; Qu, Z.G. Conjugate heat transfer in anisotropic woven metal fiber-phase change material composite. *Appl. Therm. Eng.* **2021**, *189*, 116618. [CrossRef]
26. Dimensions and Physical Characteristics of Copper Tube: Type K. Available online: [https://www.engineersedge.com/fluid\\_flow/copper\\_tubing\\_size\\_chart\\_astm\\_b88\\_13181.htm](https://www.engineersedge.com/fluid_flow/copper_tubing_size_chart_astm_b88_13181.htm) (accessed on 23 October 2022).
27. Zhang, S.; Yao, Y.; Jin, Y.; Shang, Z.; Yan, Y. Heat transfer characteristics of ceramic foam/molten salt composite phase change material (CPCM) for medium-temperature thermal energy storage. *Int. J. Heat Mass Transf.* **2022**, *196*, 123262. [CrossRef]
28. Ghalambaz, M.; Melaibari, A.A.; Chamkha, A.J.; Younis, O.; Sheremet, M. Phase change heat transfer and energy storage in a wavy-tube thermal storage unit filled with a nano-enhanced phase change material and metal foams. *J. Energy Storage* **2022**, *54*, 105277. [CrossRef]
29. Nield, D.A.; Bejan, A. *Convection in Porous Media*; Springer: Berlin/Heidelberg, Germany, 2006; Volume 3.
30. Yao, Y.; Wu, H. Interfacial heat transfer in metal foam porous media (MFPMP) under steady thermal conduction condition and extension of Lemlich foam conductivity theory. *Int. J. Heat Mass Transf.* **2021**, *169*, 120974. [CrossRef]
31. Zhao, C.; Wang, J.; Sun, Y.; He, S.; Hooman, K. Fin design optimization to enhance PCM melting rate inside a rectangular enclosure. *Appl. Energy* **2022**, *321*, 119368. [CrossRef]
32. Ghalambaz, M.; Aljaghtham, M.; Chamkha, A.J.; Abdullah, A.; Alshehri, A.; Ghalambaz, M. An anisotropic metal foam design for improved latent heat thermal energy storage in a tilted enclosure. *Int. J. Mech. Sci.* **2022**, *238*, 107830. [CrossRef]

33. Yao, Y.; Wu, H. Macroscale Modeling of Solid–Liquid Phase Change in Metal Foam/Paraffin Composite: Effects of Paraffin Density Treatment, Thermal Dispersion, and Interstitial Heat Transfer. *J. Therm. Sci. Eng. Appl.* **2021**, *13*, 041024. [[CrossRef](#)]
34. Yao, Y.; Wu, H.; Liu, Z. Direct simulation of interstitial heat transfer coefficient between paraffin and high porosity open-cell metal foam. *J. Heat Transf.* **2018**, *140*, 032601. [[CrossRef](#)]
35. Kamiuto, K.; San Yee, S. Heat transfer correlations for open-cellular porous materials. *Int. Commun. Heat Mass Transf.* **2005**, *32*, 947–953. [[CrossRef](#)]
36. Korti, A.I.N.; Guellil, H. Experimental study of the effect of inclination angle on the paraffin melting process in a square cavity. *J. Energy Storage* **2020**, *32*, 101726. [[CrossRef](#)]
37. Agarwal, A.; Sarviya, R. Characterization of commercial grade paraffin wax as latent heat storage material for solar dryers. *Mater. Today Proc.* **2017**, *4*, 779–789. [[CrossRef](#)]
38. Ukrainczyk, N.; Kurajica, S.; Šipušić, J. Thermophysical comparison of five commercial paraffin waxes as latent heat storage materials. *Chem. Biochem. Eng. Q.* **2010**, *24*, 129–137.
39. Zheng, H.; Wang, C.; Liu, Q.; Tian, Z.; Fan, X. Thermal performance of copper foam/paraffin composite phase change material. *Energy Convers. Manag.* **2018**, *157*, 372–381. [[CrossRef](#)]
40. Choi, S.-K.; Kim, S.-O.; Lee, T.-H.; Dohee-Hahn. Computation of the natural convection of nanofluid in a square cavity with homogeneous and nonhomogeneous models. *Numer. Heat Transf. Part A Appl.* **2014**, *65*, 287–301. [[CrossRef](#)]
41. Zienkiewicz, O.C.; Taylor, R.L.; Nithiarasu, P. *The Finite Element Method for Fluid Dynamics*, 7th ed.; Butterworth-Heinemann: Oxford, UK, 2014.
42. Bollhöfer, M.; Schenk, O.; Janalik, R.; Hamm, S.; Gullapalli, K. State-of-the-art sparse direct solvers. In *Parallel Algorithms in Computational Science and Engineering*; Springer: Berlin/Heidelberg, Germany, 2020; pp. 3–33.
43. Bollhöfer, M.; Eftekhari, A.; Scheidegger, S.; Schenk, O. Large-scale sparse inverse covariance matrix estimation. *SIAM J. Sci. Comput.* **2019**, *41*, A380–A401. [[CrossRef](#)]
44. Söderlind, G.; Wang, L. Adaptive time-stepping and computational stability. *J. Comput. Appl. Math.* **2006**, *185*, 225–243. [[CrossRef](#)]
45. Fahs, M.; Younes, A.; Makradi, A. A reference benchmark solution for free convection in a square cavity filled with a heterogeneous porous medium. *Numer. Heat Transf. Part B Fundam.* **2015**, *67*, 437–462. [[CrossRef](#)]
46. Chen, J. What Is a Neural Network? Available online: <https://www.investopedia.com/terms/n/neuralnetwork.asp#toc-what-is-a-neural-network> (accessed on 23 November 2022).
47. Bhat, S.A.; Huang, N.-F.; Hussain, I.; Bibi, F.; Sajjad, U.; Sultan, M.; Alsubaie, A.S.; Mahmoud, K.H. On the Classification of a Greenhouse Environment for a Rose Crop Based on AI-Based Surrogate Models. *Sustainability* **2021**, *13*, 12166. [[CrossRef](#)]
48. Sajjad, U.; Hussain, I.; Hamid, K.; Ali, H.M.; Wang, C.-C.; Yan, W.-M. Liquid-to-vapor phase change heat transfer evaluation and parameter sensitivity analysis of nanoporous surface coatings. *Int. J. Heat Mass Transf.* **2022**, *194*, 123088. [[CrossRef](#)]
49. Sajjad, U.; Hussain, I.; Raza, W.; Sultan, M.; Alarifi, I.M.; Wang, C.-C. On the Critical Heat Flux Assessment of Micro-and Nanoscale Roughened Surfaces. *Nanomaterials* **2022**, *12*, 3256. [[CrossRef](#)] [[PubMed](#)]